A STUDY OF WHISTLER-MODE RESONANCE-CONE EMISSIONS

by

Lei Xin

A thesis submitted in partial fulfillment
of the requirements for the Doctor of
Philosophy degree in Physics
in the Graduate College of
The University of Iowa

July 2005

Thesis Supervisor: Professor Donald A. Gurnett

Graduate College
The University of Iowa
Iowa City, Iowa

CERTIFICATE OF APPROVAL

PH.D. THESIS

This is to certify that the Ph.D. thesis of

Lei Xin

has been approved by the Examining Committee for the thesis requirement for the Doctor of Philosophy degree in Physics at the July 2005 graduation.

Thesis Committee: Donald A. Gurnett, Thesis Supervisor

Craig A. Kletzing

Robert L. Merlino

Ondrej Santolík

Frederick N. Skiff

Robert E. Yager

A STUDY OF WHISTLER-MODE RESONANCE-CONE EMISSIONS

by

Lei Xin

An Abstract

Of a thesis submitted in partial fulfillment
of the requirements for the Doctor of
Philosophy degree in Physics
in the Graduate College of
The University of Iowa

July 2005

Thesis Supervisor: Professor Donald A. Gurnett

ABSTRACT

This thesis analyzes funnel-shaped auroral hiss emissions observed in the magnetospheres of Earth, Jupiter and Saturn. Ray tracing calculations based on whistler-mode wave propagation near the resonance-cone are performed for several different examples to locate the source of the resonance-cone emissions generated by magnetic field-aligned electron beams.

Analysis of two terrestrial auroral hiss events observed by the Polar satellite near the south pole of the Earth found source positions at altitudes and the invariant latitudes of (2767 km, 71^{o}) and (2857 km, 78^{o}), respectively.

Ray tracing analyses of whistler-mode auroral hiss emissions observed near Jupiter's moon Io show that the radiation originates very close to the surface of Io. The inferred direction of the electron beam generating the emissions is consistent with the direction of the current predicted by the unipolar inductor model of the Io-Jupiter interaction.

Jovian auroral hiss emissions observed by the Galileo spacecraft in the Io plasma torus have also been analyzed. The computed source region is very close to the auroral hiss source region observed by the Voyager 1 spacecraft in 1979. A mechanism for the production of the electron beams responsible for the emissions is discussed.

Auroral hiss emissions observed by the Cassini spacecraft during its initial pass over the rings of Saturn on July 1, 2004 have been analyzed. By applying an appropriate electron density model, ray-tracing calculations were performed assuming that the emission is propagating in the whistler-mode near resonance cone. It was found that the source that gives the best fit to the funnel-shaped envelope of the auroral hiss is located

very close to the ring plane at a radial distance of about 1.78 R_S from the center of Saturn. The electron beam that generates the emissions is believed to be generated by a current system induced by the differential velocity between the ring particles and the co-rotating magnetosphere of Saturn.

ACKNOWLEDGMENTS

Most of all I would like to express my sincere gratitude to my advisor, Professor Donald Gurnett, who provided the initial concept for this project. Without his instructions and patience I could not have been able to complete this thesis.

I would also like to thank Joe Groene and Ann Persoon, who assisted with the plots of the spectrograms and several of the illustrations.

My thanks also go to Kathy Kurth, who helped format this thesis.

Finally, I would like to thank my wife and parents. Without their devotion and sacrifice, I would not have had a chance to study here.

TABLE OF CONTENTS

LIST OF FIGURES

I. INTRODUCTION

Auroral hiss is a type of whistler-mode radio emission that is commonly observed over the Earth's auroral zone. Auroral hiss has also been detected in the magnetospheres of Jupiter and Saturn. The frequency of auroral hiss is always below the local electron plasma frequency or electron cyclotron frequency, whichever is smaller. The frequency-time spectrum of auroral hiss often has a funnel-shaped low frequency cutoff. The funnel-shaped frequency-time characteristic is believed to be a propagation effect caused by propagation near the whistler-mode resonance cone. Substantial evidence exists that auroral hiss is produced by low energy (several eV to several keV) beams of electrons via a coherent Cerenkov radiation mechanism.

Ground-based observations of very-low-frequency radio emissions thought to be associated with the aurora were first reported by Martin *et al*. [1960]. The first comprehensive spacecraft observations of auroral hiss were made by a very-low-frequency radio receiver on the Injun 3 satellite [Gurnett, 1964]. Later in a more comprehensive study Gurnett [1966] showed that very-low-frequency radio emissions, now commonly called auroral hiss, were observed on almost every pass over the auroral zone at L values from 6 to 10. From the frequency range of the emissions, which is below the electron plasma frequency and electron cyclotron frequency, it was known that the auroral hiss is propagating in whistler-mode. The whistler-mode is a mode of propagation first analyzed by Storey [1953] to explain a lightning generated phenomena known as a whistler. Terrestrial auroral hiss can propagate either upward, usually called 'saucers', or downward, sometimes called "V-shaped auroral hiss". Several examples of both upward and downward propagating auroral hiss observed at low altitude

($\approx$ 2,500 km) are shown in Figure 1, as detected by Injun 5 satellite [Gurnett and Frank, 1972]. Another example of an auroral hiss event observed at high altitude ($\approx$ 20,000 km) by the DE-1 spacecraft over the Earth's auroral zone is shown in Figure 2 (reprinted from Gurnett *et al.* [1983]). The radiation in this case is propagating upward from a source at a much lower altitude. The events in both Figures 1 and 2 all exhibit the characteristic 'funnel-shaped' frequency-time spectrum that is characteristic of this type of radiation. The funnel shape is due to whistler-mode propagation at wave normal angles near the resonance cone. Gurnett *et al*. [1983] showed that auroral hiss is generated by a spatially localized source at a radial distance between about 1.7 and 1.9 R_E. They suggested that the upward and downward propagating auroral hiss were produced by upgoing and downward magnetic-field-aligned beams of low-energy electrons. The radiation is believed to be produced via a coherent plasma instability associated with the Landau resonance at $\upsilon_{//} = \omega / k_{//}$.

Auroral hiss has also been observed in the Jovian magnetosphere. The first Jovian auroral hiss event was detected by the Voyager 1 spacecraft near Jupiter's Io plasma torus [Gurnett and Kurth, 1979]. The Jovian auroral hiss showed a funnel-shaped low frequency cutoff that is very similar to the cutoff of auroral hiss commonly observed in the Earth's auroral regions. By analogy with Earth-based observations, it was suggested that the radiation is generated by electrons with energies from about 10eV to 1keV and fluxes in the range 10^8 to 10^{10} electrons $cm^{-2}sec$. More recently, Ulysses made observations of auroral hiss at high magnetic latitudes in the magnetosphere of Jupiter [Farrell *et al*., 1993]. Based on the high latitude of the source, the authors believed that the radiation originates from field-aligned currents induced by the solar-wind interaction with Jupiter and not by the Io-Jupiter interaction.

Before proceeding a detailed analysis of the events selected for this study it is useful to briefly discuss how auroral hiss is produced. The Injun 5 satellite provided the first direct evidence that auroral hiss is generated by intense fluxes, 10^4 to 10^7 electrons cm^{-2}sec, of low-energy electrons with energies on the order of 100eV to several keV [Gurnett and Frank, 1972]. Lin *et al.* [1984] later found that in the dayside auroral zone the auroral hiss is associated with low-energy electron beams with energies of about 100eV. Further evidence that auroral hiss is produced by electron beams was provided by a Spacelab 2 electron beam experiment [Farrell and Gurnett, 1988). In that experiment, an artificial electron beam with energy of 1 keV and current of 50 mAmp was ejected from the Space Shuttle while a spacecraft called the Plasma Diagnostics Package (PDP) detected the radiation emitted by the beam at distances of a few hundred meters. A spectrogram showing the plasma wave electric field intensities detected by the PDP is shown in Figure 3 as the spacecraft through near the beam. An obvious funnel-shaped emission pattern can be seen centered on the beam. Ray path calculation made by Gurnett *et al.* [1986] confirmed that the emission generated by the beam is propagating outward from the shuttle near the whistler-mode resonance cone, which is a cone of directions relative to the magnetic field along which the index of refraction becomes very large. Early studies of auroral hiss suggested that the radiation might be produced by an incoherent Cerenkov radiation mechanism [Taylor and Shawhan, 1974]. However, calculation based on the incoherent Cerenkov mechanism showed that the computed radiated power is much lower than the measured power [Farrell and Gurnett, 1988]. The relatively high intensities of auroral hiss indicate that a coherent plasma instability mechanism must be involved in the generation of the radiation. Farrell *et al.* [1989] showed that a coherent bunching instability could generate the observed intensities.

II. THEORY OF WHISTLER-MODE WAVE PROPAGATION

In this chapter, the general cold plasma wave dispersion relation is derived from Maxwell's equations and the equations of motion of the charged particles in the plasma. The direction of the ray path relative to an external imposed zero order magnetic field is derived for whistler- mode wave propagating near the resonance cone. This relationship is then used to explain the funnel-shaped low-frequency cutoff of auroral hiss.

2.1 Derivation of the General Dispersion Relation

To derive the general dispersion relation for small amplitude waves propagating in a cold plasma it is useful to start with the "microscopic" and "macroscopic" forms of Ampere's and Faraday's laws which are given below.

	Microscopic	Macroscopic
Ampere's Law	$\nabla \times \vec{B} = \mu_0 \vec{J} + \varepsilon_0 \mu_0 \dfrac{\partial \vec{E}}{\partial t}$	$\nabla \times \vec{H} = \dfrac{\partial \vec{D}}{\partial t}$
Faraday's Law	$\nabla \times \vec{E} = -\dfrac{\partial \vec{B}}{\partial t}$	$\nabla \times \vec{E} = -\dfrac{\partial \vec{B}}{\partial t}$

(2.1.1)

In the microscopic approach all of the charges and currents are due to "real" charges and currents, whereas in the macroscopic approach we count all of charges in the plasma as polarization charges and all the currents as displacement currents $\partial \vec{D} / \partial t$.

To relate these two approaches we introduce the conductivity tensor $\overleftrightarrow{\sigma}$, defined by $\tilde{\tilde{\vec{J}}} = \overleftrightarrow{\sigma} \bullet \tilde{\tilde{\vec{E}}}$, and the dielectric tensor $\overleftrightarrow{K}$, defined by $\tilde{\tilde{\vec{D}}} = \varepsilon_0 \overleftrightarrow{K} \bullet \tilde{\tilde{\vec{E}}}$. Here the current density is $\tilde{\tilde{\vec{J}}} = \sum_s n_s e_s \tilde{\tilde{\vec{v}}}_s$. After taking the space-time Fourier transformations of the microscopic and macroscopic forms of Ampere's law, one obtains

$$i\vec{k}\times\tilde{\tilde{\vec{B}}}=\mu_0\vec{\vec{\sigma}}\bullet\tilde{\tilde{\vec{E}}}+\varepsilon_0\mu_0(-i\omega)\tilde{\tilde{\vec{E}}} \qquad \text{and} \qquad ik\times\tilde{\tilde{\vec{B}}}=\varepsilon_0\mu_0(-i\omega)\overleftrightarrow{K}\bullet\tilde{\tilde{\vec{E}}}\,.$$

Equating the two equations gives the relationship between the dielectric tensor and the conductivity tensor:

$$\overleftrightarrow{K}=\overleftrightarrow{1}-\frac{\overleftrightarrow{\sigma}}{i\varepsilon_0\omega}\,.$$

Faraday's and Ampere's laws then become

$$i\vec{k}\times\tilde{\tilde{\vec{E}}}=-(-i\omega)\tilde{\tilde{\vec{B}}} \qquad \text{and} \qquad i\vec{k}\times\tilde{\tilde{\vec{B}}}=-\frac{i\omega}{c^2}\overleftrightarrow{K}\bullet\tilde{\tilde{\vec{E}}}\,.$$

Eliminating $\tilde{\tilde{\vec{B}}}$ between these two equations gives a homogeneous equation for the electric field

$$\vec{k}\times(\vec{k}\times\tilde{\tilde{\vec{E}}})+\frac{\omega^2}{c^2}\overleftrightarrow{K}\bullet\tilde{\tilde{\vec{E}}}=0\,.$$

By introducing the index of refraction via the definition $\vec{n}=c\vec{k}/\omega$ the above equation can be expressed in the simple form

$$\vec{n}\times(\vec{n}\times\tilde{\tilde{\vec{E}}})+\overleftrightarrow{K}\bullet\tilde{\tilde{\vec{E}}}=0\,. \qquad (2.1.2)$$

It can also be written in matrix form as $\overleftrightarrow{D}\bullet\tilde{\tilde{\vec{E}}}=0$. A non-trivial solution for $\tilde{\tilde{\vec{E}}}$ exists if and only if the determinate of the matrix $\overleftrightarrow{D}$ is zero, which gives the dispersion relation. The electric field eigenvector associated with each root of the dispersion relation can be obtained from the homogeneous equations (2.1.2), and the corresponding magnetic field eigenvector can be obtained from Faraday's law $\tilde{\tilde{\vec{B}}}=(\vec{k}/\omega)\times\tilde{\tilde{\vec{E}}}$ or $c\tilde{\tilde{\vec{B}}}=\vec{n}\times\tilde{\tilde{\vec{E}}}$.

2.2 Waves in Cold Uniform Magnetized Plasma

Next we consider the case of cold plasma with an externally imposed static uniform magnetic field $\vec{B}_0 = B_0 \hat{z}$. The linearized equation of motion for a single particle of species s is given

$$m_s \frac{d\vec{v}_s}{dt} = e_s \left[\vec{E}_1 + \vec{v}_1 \times \vec{B}_0 \right]. \tag{2.2.1}$$

After Fourier transforming, the above equation becomes

$$\begin{aligned} -i\omega m_s \tilde{v}_{sx} &= e_s \left[\tilde{E}_x + \tilde{v}_{sy} B_0 \right] \\ -i\omega m_s \tilde{v}_{sy} &= e_s \left[\tilde{E}_y - \tilde{v}_{sx} B_0 \right] \\ -i\omega m_s \tilde{v}_{sz} &= e_s \tilde{E}_z . \end{aligned} \tag{2.2.2}$$

By introducing the cyclotron frequency, $\omega_{cs} = e_s B_0 / m_s$ the above equations can be written in matrix form as

$$\begin{bmatrix} -i\omega & -\omega_{cs} & 0 \\ \omega_{cs} & -i\omega & 0 \\ 0 & 0 & -i\omega \end{bmatrix} \begin{bmatrix} \tilde{v}_{sx} \\ \tilde{v}_{sy} \\ \tilde{v}_{sz} \end{bmatrix} = \frac{e_s}{m_s} \begin{bmatrix} \tilde{E}_x \\ \tilde{E}_y \\ \tilde{E}_z \end{bmatrix}. \tag{2.2.3}$$

Solving for $\tilde{v}_{sx}$, $\tilde{v}_{sy}$ and $\tilde{v}_{sz}$ gives

$$\begin{bmatrix} \tilde{v}_{sx} \\ \tilde{v}_{sy} \\ \tilde{v}_{sz} \end{bmatrix} = \frac{e_s}{m_s} \begin{bmatrix} \frac{-i\omega}{\omega_{cs}^2 - \omega^2} & \frac{\omega_{cs}}{\omega_{cs}^2 - \omega^2} & 0 \\ \frac{-\omega_{cs}}{\omega_{cs}^2 - \omega^2} & \frac{-i\omega}{\omega_{cs}^2 - \omega^2} & 0 \\ 0 & 0 & \frac{i}{\omega} \end{bmatrix} \begin{bmatrix} \tilde{E}_x \\ \tilde{E}_y \\ \tilde{E}_z \end{bmatrix}. \tag{2.2.4}$$

The current $\tilde{\vec{J}} = \sum_s n_s e_s \tilde{\vec{v}}_s$ then becomes

$$\begin{pmatrix} \tilde{J}_x \\ \tilde{J}_y \\ \tilde{J}_z \end{pmatrix} = \sum_s \frac{n_{s0} e_s^2}{m_s} \begin{pmatrix} \frac{-i\omega}{\omega_{cs}^2 - \omega^2} & \frac{\omega_{cs}}{\omega_{cs}^2 - \omega^2} & 0 \\ \frac{-\omega_{cs}}{\omega_{cs}^2 - \omega^2} & \frac{-i\omega}{\omega_{cs}^2 - \omega^2} & 0 \\ 0 & 0 & \frac{i}{\omega} \end{pmatrix} \begin{pmatrix} \tilde{E}_x \\ \tilde{E}_y \\ \tilde{E}_z \end{pmatrix}. \tag{2.2.5}$$

Comparing with $\tilde{\vec{J}} = \vec{\vec{\sigma}} \bullet \tilde{\vec{E}}$, we can see that conductivity tensor is given by

$$\vec{\vec{\sigma}} = \sum_s \frac{n_{s0} e_s^2}{m_s} \begin{pmatrix} \frac{-i\omega}{\omega_{cs}^2 - \omega^2} & \frac{\omega_{cs}}{\omega_{cs}^2 - \omega^2} & 0 \\ \frac{-\omega_{cs}}{\omega_{cs}^2 - \omega^2} & \frac{-i\omega}{\omega_{cs}^2 - \omega^2} & 0 \\ 0 & 0 & \frac{i}{\omega} \end{pmatrix}. \tag{2.2.6}$$

Finally, the dielectric tensor can be written in the form

$$\vec{\vec{K}} = \begin{bmatrix} S & -iD & 0 \\ iD & S & 0 \\ 0 & 0 & P \end{bmatrix}, \tag{2.2.7}$$

where the quantities S, D, and P are defined as

$$S = 1 - \sum_s \frac{\omega_{ps}^2}{\omega^2 - \omega_{cs}^2}, \qquad D = \sum_s \frac{\omega_{cs}\omega_{ps}^2}{\omega(\omega^2 - \omega_{cs}^2)}, \qquad P = 1 - \sum_s \frac{\omega_{ps}^2}{\omega^2}$$

and we have introduced the plasma frequency, ω_{ps}, via the definition $\omega_{ps}^2 = \dfrac{n_{s0}e_s^2}{\varepsilon_0 m_s}$.

Following Stix [1992], the terms S and D can be decomposed into a sum and difference using the relation

$$S = \frac{1}{2}(R + L) \quad \text{and} \qquad D = \frac{1}{2}(R - L),$$

where R and L are defined by

$$R = 1 - \sum_s \frac{\omega_{ps}^2}{\omega(\omega + \omega_{cs})} \qquad \text{and} \qquad L = 1 - \sum_s \frac{\omega_{ps}^2}{\omega(\omega - \omega_{cs})}.$$

Without loss of generality, the index of refraction vector can be written $\vec{n} = (n\sin\theta,\ 0,\ n\cos\theta)$. The homogeneous equation (2.1.2) is then given by

$$\begin{bmatrix} S - n^2\cos^2\theta & -iD & n^2\sin\theta\cos\theta \\ iD & S - n^2 & 0 \\ n^2\sin\theta\cos\theta & 0 & P - n^2\sin^2\theta \end{bmatrix} \begin{bmatrix} \tilde{E}_x \\ \tilde{E}_y \\ \tilde{E}_z \end{bmatrix} = 0. \tag{2.2.8}$$

This equation has nontrivial solution if and only if the determinant of the matrix is zero, which gives the dispersion relation

$$\begin{aligned} D(\vec{n},\omega) = {} & n^2 \sin\theta\cos\theta[-(S - n^2)n^2 \sin\theta\cos\theta] \\ & + [P - n^2\sin^2\theta][(S - n^2)(S - n^2\cos^2\theta) - D^2] = 0 \end{aligned}$$

which can be written

$$D(\vec{n},\omega) = An^4 - Bn^2 + RLP = 0. \tag{2.2.9}$$

where $A = S\sin^2\theta + P\cos^2\theta$ and $B = RL\sin^2\theta + PS(1+\cos^2\theta)$. Using the quadratic formula the solution to the above equation can be written in the form

$$n^2 = \frac{B \pm F}{2A} = \frac{RL\sin^2\theta + PS(1+\cos^2\theta) \pm \sqrt{(RL-PS)^2\sin^4\theta + 4P^2D^2\cos^2\theta}}{2(S\sin^2\theta + P\cos^2\theta)}, \quad (2.2.10)$$

where $F^2 = (RL-PS)^2\sin^4\theta + 4P^2D^2\cos^2\theta$.

If we use $1 = \sin^2\theta + \cos^2\theta$ and sort out the $\sin^2\theta$ and $\cos^2\theta$ terms in the equation (2.2.9), we can get the "tangent" form of the dispersion relation, which is given by

$$\tan^2\theta = \frac{-P(n^2-R)(n^2-L)}{(Sn^2-RL)(n^2-P)}. \quad (2.2.11)$$

2.3 Origin of the Funnel-Shape Emission

As describe earlier, it is believed that auroral hiss is propagating at wave normal angles very close to the resonance cone. The resonance cone is defined as the locus of points where the index of refraction goes to infinity. The corresponding wave normal angle, θ_{Res}, is called the resonance cone angle. It can be shown that the wave fields become quasi-electrostatic near the resonance cone. From very general considerations [Gurnett and Bhattacharjee, 2005], it can be shown that the ray path direction, Ψ_{Res}, is perpendicular to the index of refraction surface, which near the resonance cone makes an angle $\psi_{\mathrm{Res}} = \pi/2 - \theta_{\mathrm{Res}}$ with respect to the magnetic field. From (2.2.11), one can see that for large n, the resonance cone angle is given by $\tan^2\theta_{\mathrm{Res}} = -\frac{P}{S}$, where

$P = 1 - \sum_s \frac{\omega_{ps}^2}{\omega^2}$ and $S = 1 - \sum_s \frac{\omega_{ps}^2}{\omega^2 - \omega_{cs}^2}$. Because of their large mass, for auroral hiss ion effects are usually negligible since the ion plasma frequency and the ion cyclotron frequency are much lower than the wave frequency. In this case, it is straight forward to show that the angle $\psi_{\mathrm{Re}s}$ is given by

$$\cos^2 \psi_{\mathrm{Re}s} = \frac{(f_c^2 - f^2)(f_p^2 - f^2)}{f_c^2 f_p^2}, \tag{2.3.1}$$

where f_p and f_c are the electron plasma frequency and cyclotron frequency, respectively.

The above expression shows, first, that the wave frequency must be lower than the minimum of the electron cyclotron frequency and the electron plasma frequency, otherwise there is no solution; and second, that the higher frequencies have larger angels of propagation. As the spacecraft approaches the magnetic field line that passes through the source, the higher emission frequencies are received first followed by the lower frequencies. Similarly, if a spacecraft departs from a source, it receives emission with gradually increasing frequency. This leads to the characteristic funnel-shaped frequency-time spectrum. Figure 4 shows three polar plots of the index of refraction surface $n(\theta)$ at frequencies f_1, f_2 and f_3. Figure 5 illustrates how the whistler mode produces the funnel-shaped frequency-time spectrum.

In practice auroral hiss usually does not have the perfect funnel-shaped spectrum shown in Figure 3. Two extreme cases can be considered. First, if the trajectory of a spacecraft passes perpendicular to the magnetic field line through the source, then the spectrogram will have a perfect symmetric funnel shape as shown in Figure 3. However, if the trajectory of the spacecraft makes a substantial angle with respect to the magnetic field line through the source, then an asymmetric funnel-shaped spectrogram is obtained with one side having longer duration. This is a possible explanation for single-sided funnel-shaped auroral hiss emissions that are sometimes seen. Second, the shape of the low frequency cutoff depends on the distance of closest approach to the magnetic field line through the source. If the distance of closest approach is large, the low frequency cutoff develops an upward directed parabolic shape near the point of closest approach.

2.4 Ray Path Tracing

Ray tracing is an important tool for locating the source of auroral hiss. Recall that the ray path makes an angle $\psi_{\mathrm{Re}s}$ with the magnetic field and that this angle is given by

$$\cos^2\psi_{\mathrm{Re}s} = \frac{(f_c^2 - f^2)(f_p^2 - f^2)}{f_c^2 f_p^2}.$$

In order to find the direction of a ray path, we need the cutoff frequency f, the plasma frequency f_p, the cyclotron frequency f_c.

Since the cutoff frequency is the low frequency boundary of the emission, the electric field spectrum for a specific universal time is used to find the cutoff frequency. As shown in Figure 6 the dramatic decrease in the intensity at the cutoff gives the cutoff frequency at that time (i.e., the vertical line).

The cyclotron frequency is directly related to the magnetic field and is given by $f_{ce} = 28B[H_z]$. The magnetic field can be calculated from on-board magnetic field measurements or from standard planetary magnetic field models. A planetary magnetic field is often described as the gradient of a scalar potential [Kivelson and Russell, 1995]:

$$\vec{B} = -\vec{\nabla}\Phi = -\vec{\nabla}(\Phi^i + \Phi^e),$$

where Φ^i is the magnetic scalar potential due to internal source of the planet, and Φ^e is the scalar potential due to external source. Both of these potentials can be expressed by a sum of associated Legendre polynomials:

$$\Phi^i(r,\theta,\varphi) = a\sum_{n=1}^{\infty}\sum_{m=0}^{n}[r/a]^{-n-1}P_n^m(\cos\theta)\left(g_n^m\cos(m\varphi)+h_n^m\sin(m\varphi)\right)$$

and

$$\Phi^e(r,\theta,\varphi) = a\sum_{n=1}^{\infty}\sum_{m=0}^{n}[r/a]^{n}P_n^m(\cos\theta)\left(G_n^m\cos(m\varphi)+H_n^m\sin(m\varphi)\right)$$

where a is the planet's radius, and θ and φ are the colatitude and east longitude, respectively, in geophysical coordinates. The $P_n^m(\cos\theta)$ terms are associated Legendre functions with Schmidt normalization

$$P_n^m(\cos\theta) = N_{nm}\left(1-\cos^2\theta\right)^{m/2} d^m P_n(\cos\theta)/d(\cos\theta)^m,$$

where $P_n(\cos\theta)$ is the Legendre function, and $N_{nm} = 1$ when $m = 0$, and $[2(n-m)!/(n+m)!]^{\frac{1}{2}}$ otherwise. The coefficients g_n^m, h_n^m, G_n^m, and H_n^m are chosen to minimize the difference between the model field and observations. For example, The International Geomagnetic Reference Field (IGRF) model coefficients for the Earth are based on all available data sources including geomagnetic measurements from observatories, ships, aircraft and satellites. In most cases, near the planet the magnetic dipole term provides a good approximation to a planetary magnetic field. In a spherical coordinates with the magnetic moment along the $z-$axis, the magnetic field of a magnetic dipole can be expressed as

$$B_r = 2Mr^{-3}\cos\theta$$
$$B_\theta = Mr^{-3}\sin\theta$$
$$B = Mr^{-3}\left(1+3\cos^2\theta\right)^{\frac{1}{2}}$$

where θ is the magnetic colatitude as defined in Figure 7, and M is the dipole magnetic moment. In Cartesian coordinates, the three components of the magnetic field are

$$\begin{aligned} B_x &= 3xzM_z r^{-5} \\ B_y &= 3yzM_z r^{-5} \\ B_z &= \left(3z^2 - r^2\right) M_z r^{-5} \end{aligned} \quad .$$

A magnetic field line consists of points through which the tangent line is along the magnetic field direction. Thus,

$$r d\theta / B_\theta = dr / B_r \ .$$

By integrating the above equation the equation of a field line can be obtained and is given by

$$r = r_0 \sin^2 \theta \ ,$$

where r_0 is the distance to the equatorial crossing of the field line. The equation can also be written in terms of L (measured in planetary radii) and the magnetic latitude λ:

$$r = LR \cos^2(\lambda) \ .$$

Another term commonly used to characterize the magnetic field line is the invariant latitude. It is the latitude where a field line crosses the surface of the planet. The relation between L and invariant latitude Λ is given by

$$\cos \Lambda = \left(\frac{1}{L}\right)^{\frac{1}{2}} .$$

The plasma frequency can be computed from the electron density by using the formula $f_p = 8980\sqrt{n_e} H_z$, where n_e is the electron density in cm^{-3}. Persoon *et al.* [1983] found, by tracing the upper cutoff of auroral hiss, that the electron density at high altitudes over the Earth's polar region varies with the radial distance as $n_e \propto r^{-3.85}$. A more general density profile that works well at both high and lower altitudes is given by Kletzing and Torbert [1994]

$$n(r) = n_0 e^{-(r-r_0)/h} + n_1 (r-1)^{-1.55},$$

where n is in cm^{-3} and r is measured in Earth radii, R_E, from the center of the Earth. The first term represents the exponential decreases of the electron density in the ionosphere with height. The second term comes from the magnetospheric component. The best fit of the model to data yields the following parameters: $n_0 = 6\times10^4$, $r_0 = 1.05$, $h = 0.06$, $n_1 = 17$.

Since the plasma frequency at in the Io torus is usually much larger than the electron cyclotron frequency and the wave frequency, the ray path angle can be simplified to

$$\sin\Psi_{\mathrm{Res}} = \frac{f}{f_c}. \tag{2.4.1}$$

Therefore, using either (2.3.1) or (2.4.1) the angle ψ_{Res} can be calculated. The ray path is traced backward from the trajectory of the spacecraft to the source as follows (refer to Figure 8). For any point P_0 on the trajectory in which the funnel-shaped cutoff is observed, the angle ψ_{Res} is computed by formula (2.3.1) or (2.4.1). The new point P_1 on the ray path is obtained by advancing by a small increment along the ψ_{Res} direction. The plasma density and magnetic field is then recalculated at P_1, giving a new value of angle ψ_{Res}. The same procedure gives P_2, and the process is repeated. This procedure continues until the ray path extends far enough to intersect with other ray paths. If the ray paths for different frequencies intersect at a common point or a small region this intersection is considered to be the source region. If the Poynting vector of the wave is not measured, two directions of propagation become possible. In this case, the ray paths may converge to two possible source regions. Such a case is demonstrated in Figure 8.

III. AURORAL HISS EMISSIONS OBSERVED BY THE POLAR SPACECRAFT

As the Polar spacecraft passes over the Earth's polar region, two funnel-shaped auroral hiss features are usually observed, one at each of the two crossings of the auroral zone. A typical example is shown in Figure 9, which shows the electric field spectrogram of an auroral hiss event observed over the southern hemisphere on Aug. 27, 1996. Since the trajectory (refer to Figure 10) of the spacecraft is approximately symmetric to the magnetic axis as the pair of emission cutoffs is observed, two independent sources, one located on the left of the magnetic axis, the other located on the right of the magnetic axis, must exist. By using a density model given by Kletzing and Torbert [1994], ray tracing has been performed for several different emission frequencies. It is found that these rays converge to two source positions with the altitudes and the invariant latitudes of (2767 km, 71^{o}) and (2857 km, 78^{o}), respectively. Figure 10 shows the ray paths for five different frequencies propagating from the two sources. Gurnett *et al.* [1983] found that the source position of an auroral hiss event observed by DE-1 spacecraft was at an altitude between 4500 km and 5700 km with invariant latitude about 65^{o}. Another auroral hiss event observed by DE-1 has been analyzed by Lin *et al.* [1984]. They obtained a source position at an altitude of 7000 km and an invariant latitude near 73^{o}. The auroral hiss event analyzed here places the source region at an altitude that is significantly lower than those observed by DE-1. We conclude that the source region of upgoing auroral hiss can be at least as low as 2800 km. Since the detection of auroral hiss indicates the existence of a low-energy electron beam, the auroral hiss event observed by Polar shows that up-going electron beams can be accelerated at an altitude of about 2800 km. FAST satellite has frequently observed up-going electron beams at altitudes between 2000 and 4000 km [Carlson *et al.*, 1998].

IV. AURORAL HISS NEAR JUPITER'S MOON IO

4.1 Observations

The Galileo spacecraft, which was placed in the orbit around Jupiter on Dec 7, 1995, carried out a series of close flybys of the Jupiter's moon, Io. Figure 11 shows the spacecraft trajectory relative to Io for one such flyby, which occurred on Oct 16, 2001 during orbit 32. This flyby was the sixth close flyby of Io. In this figure, an Io-centered coordinate system is used with the +z axis aligned parallel to Jupiter's rotational axis and the +x axis aligned parallel to the nominal co-rotational plasma flow induced by Jupiter's rotation. The +y axis completes the usual right-handed coordinate system. As can be seen, the spacecraft passed over the south pole of Io with a closest approach radial distance of about 2000 km at 0123:20 UT.

A spectrogram of the electric field intensities obtained from the Galileo plasma wave instrument in the vicinity of Io during this flyby is shown in Figure 12. The red color in the spectrum represents the strongest emission while the blue color represents the weakest emission. The dynamic range from dark blue to bright red is 70 db. The time range, from 0108:00 to 0138:00UT, has been chosen so that the auroral hiss emission can be shown clearly. The emission spans a frequency range from about 1 to 40 kHz, and has an asymmetrical funnel-shaped low-frequency cutoff that decreases monotonically from about 40 kHz at 0116:00UT to about 1 kHz at 0121:00UT. The electron cyclotron frequency, shown by the white line marked f_{ce}, was computed from on-board magnetic field measurements [Kivelson *et al.*, 1996]. The electron cyclotron frequency is about 58 kHz and the proton cyclotron frequency is about 32Hz. The electron plasma frequency, shown by the white line marked f_{pe}, is about 600 kHz during the period of interest. As can be seen, the following inequalities exist among the proton cyclotron frequency f_{ci}, the observed emission frequency f, the electron cyclotron frequency f_{ce}, and the electron plasma frequency f_{pe}:

$$f_{ci} << f << f_{ce} < f_{pe} \quad (4.1.1)$$

For these parameters the only possible mode of propagation in the frequency range of interest is the whistler mode [Gurnett and Bhattacharjee, 2005]. As will be shown shortly these inequalities allow us to greatly simplify the cold plasma dispersion relation, which will be used later to perform ray-path calculations.

Figure 13 shows plots of the x, y, and z components of the magnetic field in nT for the same time range shown in Figure 12. From these plots, it can be seen that all three components of the magnetic field are smooth and slowly varying except in the interval between 0115:00 and 0132:00UT, which corresponds to the time range when the spacecraft was in the vicinity of Io (comparing with Figure 11). In this interval large perturbations are clearly observed in the B_x and B_y plots with amplitudes of about $\Delta B_x \approx 600$ nT (relative to a background of –300 nT) and $\Delta B_y \approx 300$ nT (relative to a background of -300nT). Obvious abrupt changes in magnetic field occurred at about 0121:00 and 0129:00UT. According to Ampere's law $\nabla \times \vec{B} = \mu_0 \vec{J}$, those changes indicate that the spacecraft crossed two intense current sheets, one near the inner boundary of Io, and the other near the outer boundary of Io. In the region between the two major current sheets the z-component of magnetic field increased (decreased in magnitude) gradually with some small fluctuations. After the second current sheet crossing the B_z field drops down to an equilibrium value of about -1650nT, which is slightly larger than the field (-1900nT) that was present during the approach to Io. Comparing with the electric field spectrum, it can be seen that the auroral hiss emission started when the magnetic perturbation started. The vertex of the funnel-shaped emission occurs almost exactly at the same time as the first major magnetic field discontinuity. These facts can be explained as follows: when the spacecraft approached the current sheet auroral hiss emission generated by the current was first detected; the radiation was continuously received with the largest intensities occurring when the spacecraft was in the center of the current sheet. These data suggest that the auroral hiss is closely associated with the current that causes the discontinuity in the magnetic field. This fact gives further evidence of the presence of a field-aligned current flow connecting Io with Jupiter as proposed by Goldreich and Lynden-Bell [1969]. Similar magnetic perturbations of ~5% were also detected earlier by the Voyager 1 magnetometer when the spacecraft crossed Io's magnetic flux tube about $11R_{Io}$ south of Io [Ness *et al*., 1979].

4.2 The Unipolar Inductor Model

In order to explain the origin of the field-aligned current, which is believed to be responsible for the auroral hiss emission observed during the Io flyby on orbit 32, it is useful to briefly discuss the so called "Unipolar Inductor" model of Io's interaction with the Jovian magnetosphere [Goldreich and Lynden-Bell, 1969]. In this section, we will discuss (1) Io's influence on Jupiter's decametric emission, and (2) the unipolar inductor model.

It is well known that Jupiter is an intense radio emission source, with radiation extending from decametric wavelengths [Burke and Franklin, 1955] to kilometric wavelengths [Carr *et al*., 1983]. In the process of studying the time variations of these radio emissions Bigg [1964] found that the emission pattern received on Earth is closely correlated with the geometric position of Io relative to the Earth-Jupiter line. The decametric emission intensity from 1961-1963 is shown in Figure 14 as a function of the departure of Io from superior geocentric conjunction. Superior geocentric conjunction is defined as the moment when Io is located on the far side of the Earth-Jupiter line. As can be seen from this figure the intensity of the emission is closely controlled by the position of Io, with the most intense emissions occurring when Io is about 90 and 240 degrees from superior geocentric conjunction. The probability of receiving decametric emission on Earth is almost unity at 90 and 240 degrees from superior geocentric conjunction. Thus Bigg showed that Io strongly modulates the intensity of Jupiter's decametric radiation.

The unipolar inductor model of Goldreich and Lynden-Bell is based on two assumptions: first, that the d.c. conductivity of Jupiter's magnetospheric plasma along magnetic field lines is infinite, and zero across the magnetic field lines, and second, that Io is an almost perfect conductor. Goldreich and Lynden-Bell were the first to point out that Io may act as a unipolar inductor, thereby imposing an emf of 7×10^{5} volts across its radial diameter. This emf drives a current that flows on the surface of the magnetic flux tube connecting Io with Jupiter. The geographical co-latitude for the northern foot of the Io flux tube is $\theta_i = 24^{\circ}$. The current starts from the outer face of Io, flows to Jupiter's ionosphere along one-half of the flux tube, crosses the magnetic field in Jupiter's ionosphere, and then flows back to Io along the other half of the flux tube, thereby closing the current loop. Figure 15 illustrates this current loop. The total current is about 10^{6}amp and is carried by keV electrons which are accelerated at Io and Jupiter's ionosphere by parallel electric fields. The decametric emission is believed to be produced by coherent cyclotron radiation from these electrons. The auroral hiss emission observed in Figure 12 is believed to be generated by the accelerated electron beam at Io. Confirming evidence of the existence of these field-aligned currents was provided by magnetic field measurement from the Voyager 1 magnetometer. Figure 17 shows the observed magnetic field perturbation components $\Delta B_x, \Delta B_y$, and the fitted curves for a 2D-dipole and a line current [Ness *et al*., 1979]. As can be seen the 2D-dipole source gives a quite good fit to the perturbed field.

The unipolar inductor model has been refined by Neubauer [1980]. Figure 18 demonstrates the generation of an Alfven wave by a conductor moving perpendicular to uniform magnetic field. It has been shown by Drell *et al*. [1965] that the current is not really along the magnetic field but rather is carried at an angle to the magnetic field by Alfven waves, so-called Alfven 'wings' as seen in the Io frame of reference. The angle between the direction of the Alfven wave propagation and the magnetic field is given by $\theta_A = \tan^{-1} M_A$, where M_A is the Alfven Mach number. The Alfven Mach number is defined by $M_A = U_0 / V_A$ where U_0 is the relative speed between Io and the plasma flow, and $V_A = B / \sqrt{\mu_0 \rho_m}$ is the Alfven speed. Typical parameters for Io are $U_0 \approx 56.8 km/s$, $B \approx 1900 nT$, $V_A \approx 356 km/s$, $M_A \approx 0.16$, and $\theta_A \approx 9.1^\circ$.

4.3 Model Calculation

The left-hand side of the auroral hiss emission observed by Galileo has a frequency-time shape very similar to the funnel shape predicted by the simple model shown in Figure 5. This close similarity indicates that we can use the whistler-mode propagation near the resonance cone to locate the emission source. In the following, we will locate the possible source of radiation by finding the best fit to the funnel-shaped low frequency cutoff using a more exact geometric model that takes into account the spacecraft trajectory. Initially we assume the radiation source is a simple point source. Then later we investigate the possibility that the radiation source is a sheet source aligned along magnetic field lines that are tangent to the surface of Io.

4.3.1 A Simple Model: Point Source Emission

Recall that under the assumptions $f^2 << f_p^2$ and $f_c^2 << f_p^2$ we have $\sin\psi = f / f_c$, where ψ is the angle between the limiting ray path direction and the magnetic field, f is the cutoff frequency, and f_c is the electron cyclotron frequency.

To compare the theoretical model with the observations, we first calculate the time dependence of the cutoff frequency from the magnetic field geometry relative to the spacecraft trajectory. Figure 18 shows the geometric relations needed for computing ψ, the angle between the limiting ray path and the magnetic field through the emission source: $R(x, y, z)$ is an arbitrary point on the trajectory of the Galileo; $R(x_s, y_s, z_s)$ represents the position of the emission source; $R_0(x_0, y_0, z_0)$ is a point when the spacecraft is on the magnetic line through the source. Obviously, R_0 and R_s are adjustable points. R_0 is a point where the lowest frequency of the emission of the cutoff boundary is received. By inspecting the spectrum in Figure 12, we find that the low frequency apex of the emission occurs at about 0120:00UT, which corresponds to spacecraft coordinates $(x_0, y_0, z_0) = (-0.893, 0.24, -1.019)$. Using these coordinates we fix the point R_0. Next the height of the source $h = |\vec{R}_0 - \vec{R}_s|$ is adjusted until a best-fit cutoff boundary is found. In the following we will show the detail of the calculation.

Since the perturbation of the magnetic field is much smaller than the static component, we assume a constant magnetic field. If the height of the emission source h is given, then the coordinates of the source $R(x_s, y_s, z_s)$ can be calculated by the following simple geometric relations:

$$\frac{x_0 - x_s}{B_x} = \frac{y_0 - y_s}{B_y} = \frac{z_0 - z_s}{B_z} = \frac{h}{B}.$$

Using the above relations gives the following equations,

$$x_s = x_0 - \frac{h}{B} B_x,\ y_s = y_0 - \frac{h}{B} B_y \text{ and } z_s = z_0 - \frac{h}{B} B_z .$$

Using these equations the calculation of the cutoff frequency f is straightforward. For each point in the range 0115:00 UT to 0120:00 UT (where the auroral hiss radiation occurs) on the trajectory $R(x, y, z)$, we calculate the angle ψ between $\vec{R} - \vec{R}_s$ (the limiting ray path) and $\vec{R}_0 - \vec{R}_s$ (the magnetic field line) using the equation

$$cos\,\psi = \frac{(\vec{R} - \vec{R}_S)\bullet(\vec{R}_0 - \vec{R}_S)}{\left|\vec{R} - \vec{R}_S\right|\left|\vec{R}_0 - \vec{R}_S\right|}$$
$$= \frac{(x - x_S)(x_0 - x_S) + (y - y_S)(y_0 - y_S) + (z - z_S)(z_0 - z_S)}{\sqrt{(x - x_S)^2 + (y - y_S)^2 + (z - z_S)^2}\sqrt{(x_0 - x_S)^2 + (y_0 - y_S)^2 + (z_0 - z_S)^2}}$$

Recall that the cutoff frequency is given by

$$f = f_c \sin\psi \text{, where } \sin\psi = \sqrt{1 - (\cos\psi)^2}\ .$$

Using the above equation we can compute the time dependence of the cutoff frequency $f = f(t)$ can be computed. Figure 19 shows the results for three different values of h. The solid points in the figure are sampled from the low frequency cutoff of the auroral hiss spectrum Figure 12. From Figure 19 we can see that the position of the source is located roughly between $h = 0.65$ and $h = 1.15$, here h is in the unit of the radius of Io. The wide range of h indicates that the source doesn't have a sharp defined low-altitude boundary. This is reasonable, since the emission spectrum in Figure 12 doesn't have a sharply defined frequency-time boundary. The best fit to the cutoff frequency data gives $h = 0.9$, which corresponds to the source position at coordinates $R_s(x_s, y_s, z_s) = (-1.035, 0.469, -0.16)$. The small value of z_s indicates that the source lies near the equator of Io, roughly in the region where Jupiter's magnetic field is tangent to the surface of Io. In Figure 20 the best-fit cutoff curve is drawn on the spectrogram for comparison.

4.3.2 Calculation Based on a Sheet Source

Since the frequency-time spectrum of the radiation is filled-in instead of being a sharp line, it is likely that the source of the emission is either a line or a sheet source. Applying the unipolar inductor model, we consider the possibility that the source is a cylindrical current sheet (see Figure 21). We choose the axis of the cylinder in the direction of the magnetic field line at R_0 through the center of the Io with radius $r = \sqrt{x_s^2 + y_s^2 + z_s^2}$ =1.15. The radius $r = 1.15 > 1$ is considered reasonable since the current source is most likely produced in the ionosphere of the Io and therefore somewhat above the surface. Since we have no information on the magnetic field variations away from the trajectory, we simply assume that the local current sources responsible for the radiation are also along B_0 at R_0. Also for simplicity, we draw a plane p with its normal along z direction through point R_s (the location of the point source that gives a good fit as shown in the previous calculations.). The intersection between the plane p and the cylindrical current sheet makes a curve C. For every individual point on the trajectory

$R(x,y,z)$ (See Figure 22) we draw the normal of the current cylinder $R_0^{'}R$ (Note: $R_0^{'}$ lies on the surface of the cylinder). The line $R_s^{'}R_0^{'}$ is parallel to B_0 and intersects the curve C at point $R_s^{'}$ which we took as the point source responsible for the cutoff frequency at $R(x,y,z)$. The coordinates of $R_0^{'}(x_0^{'},y_0^{'},z_0^{'})$ and $R_s^{'}(x_s^{'},y_s^{'},z_s^{'})$ can be calculated as follows:

Define the unit vector of B_0 as $\hat{n}_B$ = (a, b, c) = (0.158,-0.254,-0.954), then the coordinates of point $R_1(x_1,y_1,z_1)$ satisfy

$$\begin{aligned}
&\frac{x_1}{a}=\frac{y_1}{b}=\frac{z_1}{c}=k_1\\
&x_1=ak_1\\
&y_1=bk_1\\
&z_1=ck_{1.}
\end{aligned} \tag{4.3.2.1}$$

$$R_1R\bullet n_B=0\Rightarrow(x-x_1)a+(y-y_1)b+(z-z_1)c=0.$$

So, we have $k_1=\dfrac{ax+by+cz}{a^2+b^2+c^2}$.

Substitute k_1 into (4.3.2.1), we have $R_1(x_1,y_1,z_1)$.

The equation of line $R_1R_0^{'}R$ is

$$\begin{aligned}
&\frac{x_0^{'}-x_1}{x-x_1}=\frac{y_0^{'}-y_1}{y-y_1}=\frac{z_0^{'}-z_1}{z-z_1}=k_2\Rightarrow\\
&x_0^{'}=k_2(x-x_1)+x_1\\
&y_0^{'}=k_2(y-y_1)+y_1\\
&z_0^{'}=k_2(z-z_1)+z_1
\end{aligned} \tag{4.3.2.2}$$

where $k_2=\dfrac{r}{\sqrt{(x-x_1)^2+(y-y_1)^2+(z-z_1)^2}}$.

Substitute k_2 into (4.3.2.2), we get the coordinates of $R_0^{'}(x_0^{'},y_0^{'},z_0^{'})$.

To find $R_s^{'}(x_s^{'}, y_s^{'}, z_s^{'})$, note that $\vec{R}_0^{'} - \vec{R}_s^{'}$ is parallel to $\vec{B}_0$ so

$$\begin{aligned}
&\frac{x_s^{'} - x_0^{'}}{a} = \frac{y_s^{'} - y_0^{'}}{b} = \frac{z_s^{'} - z_0^{'}}{c} = k_3 \Rightarrow \\
&x_s^{'} = ak_3 + x_0^{'} \\
&y_s^{'} = bk_3 + y_0^{'} \\
&z_s^{'} = ck_3 + z_0^{'}
\end{aligned} \tag{4.3.2.3}$$

Recall $z_s^{'} = z_s \Rightarrow k_3 = \dfrac{z_s - z_0^{'}}{c}$

Next, substitute k_3 into (4.3.2.3), which gives the coordinates of $R_s^{'}(x_s^{'}, y_s^{'}, z_s^{'})$.

Once we have the coordinates of $R_0^{'}(x_0^{'}, y_0^{'}, z_0^{'})$ and $R_s^{'}(x_s^{'}, y_s^{'}, z_s^{'})$, we can calculate the angle ψ between $\vec{R} - \vec{R}_s^{'}$ (the limiting ray paths) and $\vec{R}_0^{'} - \vec{R}_s^{'}$ (The magnetic field line). This angle is given by

$$\cos\psi = \frac{(\vec{R} - \vec{R}_s^{'}) \bullet (\vec{R}_0^{'} - \vec{R}_s^{'})}{\left|\vec{R} - \vec{R}_s^{'}\right| \left|\vec{R}_0^{'} - \vec{R}_s^{'}\right|} = \frac{(x - x_s^{'})(x_0^{'} - x_s^{'}) + (x - x_s^{'})(y_0^{'} - y_s^{'}) + (z - z_s^{'})(z_0^{'} - z_s^{'})}{\sqrt{(x - x_s^{'})^2 + (x - x_s^{'})^2 + (z - z_s^{'})^2}\sqrt{(x_0^{'} - x_s^{'})^2 + (y_0^{'} - y_s^{'})^2 + (z_0^{'} - z_s^{'})^2}}$$

Finally, the time dependent cutoff frequency is computed using

$$f = f_c \sin\psi \text{, where } \sin\psi = \sqrt{1 - (\cos\psi)^2}\ .$$

Figure 22 shows the cutoff curve calculated by assuming a sheet emission source. The solid circles are sampled from the cutoff boundary of the spectrum of the auroral-hiss emission, while the solid line represents the best fit curve calculated above. As can be seen, the fit to the ray tracing is quite good. This indicates that the emission source responsible for the auroral-hiss emission is most likely a sheet source. The good fit also indicates that the trajectory of the spacecraft is nearly perpendicular to the cylindrical current sheet.

As can be seen from Figure 19 and Figure 22, the funnel-shaped low frequency cutoff calculated by assuming the emission source is either a point source or a cylindrical sheet source both provide a good fit to the observed auroral-hiss spectrum, which provides strong verification that the whistler mode emission is propagating at angles very close to the resonance cone, as has been assumed. The emission source has a poorly defined low-altitude boundary since the low frequency cutoff of the emission spectrum is not sharply defined.

4.4 Summary and Interpretation

Broadband auroral hiss emissions have been observed by the Galileo spacecraft near Jupiter's moon Io. The frequency range of the emission occurs well below the local electron cyclotron frequency and the local electron plasma frequency, and above the proton cyclotron frequency. The frequency range indicates that the emissions are propagating in the whistler-mode. The electric field spectrum has a funnel-shaped low frequency cutoff characteristic that is very similar to the terrestrial auroral hiss commonly observed in the Earth's auroral region. The close association of the central axis of the funnel with the onset of the magnetic field perturbation caused by Io indicates that the emission is probably generated by a current sheet originating from Io. This current sheet is most likely produced by the unipolar inductor interaction of Io with the Jovian magnetic field. Since auroral hiss is known to be produced by electron beams, these observations indicate the existence of a southward-directed field-aligned electron beam accelerated near Io. That means that the direction of the current is northward, pointing toward Io. The direction of the current agrees well with that predicted by the unipolar inductor model.

The main difference compared to terrestrial auroral hiss is that the spectrum doesn't have an obvious funnel-shaped low frequency cutoff on its right-hand branch. Since no detailed information is available on the plasma parameters in the inner and outer regions of the flux tube, one possible explanation for this asymmetry of the emission is that the plasma inside the flux tube is hot compared to the plasma outside the flux tube. High temperatures could cause the emission to be absorbed by Landau damping. The same emission is also observed at the exit of the flux tube which occurs at about 0130:00. These emissions have an upper frequency cutoff at about 15 kHz which is about three times lower than that of the emissions observed as the spacecraft approaches the flux tube. The lower frequency may indicate that the current carriers on the outer region of the flux tube have lower kinetic energy than those on the inner region of the flux tube.

Assuming that the emission is propagating in the whistler-mode near the resonance cone, the low-altitude boundary of the current source generating the emission has been derived from ray tracing calculations which give best fit to the funnel-shaped low frequency cutoff. A series of ray tracing computations have been performed by assuming a point and cylindrical sheet emission sources. It is found that the low-altitude boundary of the current source lies at near the equatorial plane of Io with coordinates $(-1.035, 0.469, -0.16)$, which corresponds to a height of about 270 km above the surface of Io. From the ionospheric electron density profile given by Kliore *et al.* [1974], we can see that the current source well lies in the ionosphere of Io with a local electron density about 3×10^4 electrons per cubic centimeter. It is also shown that the source has a rough low-altitude boundary between 0.65-1.15R_{Io} below the spacecraft along the local magnetic field line. The generation mechanism of this type of emission is commonly believed to be generated via a coherent Cerenkov mechanism. The auroral-hiss emission observed by Galileo is likely generated by electron beam accelerated by parallel electric fields in the ionosphere of Io.

V. AURORAL HISS DETECTED NEAR THE IO PLASMA TORUS

Voyager 1 made the first detection of funnel-shaped auroral hiss near the Io plasma torus. Gurnett and Kurth [1979] gave a detailed analysis of the event. They found that the source that produced the emission was located along the L=5.6 L-shell, either 0.14R_J south of the magnetic equator or 1.16R_J north of the magnetic equator. This result was later refined by Morgan *et al*. [1994]. Both of these studies found two possible source positions that were consistent with the observations. Those positions are at the north and south edges of the hot plasma torus and on the boundary between the hot and cold regions of the torus.

Figure 23 shows another auroral hiss event observed by the Galileo spacecraft on Nov 05, 2002. The trajectory of the spacecraft and ray paths of the emission for various frequencies are shown in Figure 24. The ray paths for six different cutoff frequencies converge to two possible source positions with coordinates $(\rho_{cent}, z_{cent}) = (5.51, 1.04)$ and $(\rho_{cent}, z_{cent}) = (5.06, -1.36)$ in units of R_J using the centrifugal coordinate system of Hill *et al.*, [1974], where ρ_{cent} represents the distance along the centrifugal equator and z_m the distance from the centrifugal equator. Figure 25 shows the positions of the two sources (represented by the colored stars) superimposed on a density contour map of the Io plasma torus given by Bagenal [1994]. While both sources seem to be located near the boundary between the hot and cold plasma of the torus, the northern source position is more consistent with the calculation by Morgan *et al*. [1994].

The generation of auroral implies the existence of an electron beam. Since the auroral hiss radiates toward the centrifugal equator, we deduce that the existence of electron beams directed inward, toward the centrifugal equator. This implies that there is a current directed along the field lines northward and southward from the north and south edges of the hot-cold torus boundary, respectively. This situation is shown schematically in Figure 26.

VI. OBSERVATION AND ANALYSIS OF AURORAL HISS AT SATURN

6.1 Observations

During the initial pass of the Cassini spacecraft over the rings of Saturn on July 1, 2004, a well-defined funnel-shaped electric field emission was detected by the plasma wave instrument onboard the spacecraft. This is the first detection of auroral hiss at Saturn. Figure 27 shows the electric field spectrum of the emission observed during this pass. The auroral hiss emission spans a time range from 03:10 to 03:45UT and frequencies from 1 to 12 kHz. The electric field spectral density of the emission reaches intensities as high as 10^{-12} V^2/m^2Hz. The emission has an upper cutoff at the local electron plasma frequency and an asymmetric funnel-shaped lower cutoff with a poorly defined center. The spectral emission bends up abruptly at about 03:46 UT corresponding to passage into Cassini division where particles can freely pass through the rings. Figure 28 shows a polar view of the trajectory of Cassini during the time interval the auroral hiss emission was observed. The auroral hiss emission was detected north of the equator slightly above the B ring within a latitude range of about 7^o to 13^o. These latitudes are very low compared to the high latitudes ($\sim70^o$) at which auroral hiss is observed at Earth, suggesting that the emission is somehow associated with the rings.

6.2 Ray Tracing Analyses

The funnel-shaped low frequency cutoff of auroral hiss can be explained by whistler-mode propagation near the resonance cone. In contrast to the observations of auroral hiss at Jupiter, where the electron plasma frequency is much larger than the electron cyclotron frequency, for the auroral hiss at Saturn the electron cyclotron frequency is much larger than the plasma frequency [Gurnett *et al*., 2005]. The resonance cone angle, ψ_{res} can then be approximated by

$$\tan^2 \psi_{res} = -\frac{S}{P} \approx \frac{\omega^2}{\omega_p^2 - \omega^2}, \tag{6.2.1}$$

where S and P are defined by Stix [1992]. As is usually the case, equation (6.2.1) shows that higher frequencies propagate at larger angles with respect to the magnetic field line. When the spacecraft approaches the source higher frequencies are observed first then the lower frequencies are received, thereby leading to the funnel-shaped low frequency envelope.

Equation (6.2.1) shows that the ray path direction is very dependent on the plasma frequency. This is in strong contrast to the situation at Jupiter where the ray path direction is almost completely controlled by the electron cyclotron frequency (i.e., when $f_p >> f_c$). Therefore, an appropriate electron density model is vital to the ray tracing computation. A 2-D the electron density model has been constructed based on density measurement along the trajectory with an exponential function to model the dependence on the distance from the ring plane. The ray path computation involves several steps. First, the upper cutoff frequency of the auroral hiss, which gives the electron density along the spacecraft trajectory, is fitted within time range from 0309 to 0343UT by a 4th order polynomial and an exponential function that depends on ρ, the radial distance from Saturn projected onto the equatorial plane. The best fit equation for the electron density is

$$n_0(\rho) = 245.715\rho^4 - 1611.24\rho^3 + 3968.58\rho^2 - 4353.17\rho + 1795.09 + 0.1\exp[(\rho - 1.86)/0.005]cm^{-3} \qquad (6.2.2)$$

Figure 29 shows plots of the electron density, given by the blue line and the above model fit given by red line. Second, following Moncuquet *et al*. [2005], we assume a Gaussian dependence of electron density on the distance from the equatorial plane. Three types of ions H^+, O_2^+ and O^+ with relative contributions 20%, 50% and 30%, respectively, are used, see Richardson and Jurac, [2004]. Finally, assuming plasma charge neutrality the electron density $n(\rho, z)$ is modeled by the following formula

$$n(\rho, z) = \frac{n_0(\rho)}{\left[0.2\exp(-\frac{z_{traj}^2}{H_1^2}) + 0.5\exp(-\frac{z_{traj}^2}{H_2^2}) + 0.3\exp(-\frac{z_{traj}^2}{H_3^2})\right]} \times \left[0.2\exp(-\frac{z^2}{H_1^2}) + 0.2\exp(-\frac{z^2}{H_2^2}) + 0.3\exp(-\frac{z^2}{H_3^2})\right]cm^{-3}, \qquad (6.2.3)$$

where $n_0(\rho)$ is given by equation (6.2.2). The terms H_1, H_2 and H_3 represent the scale heights of H^+, O_2^+ and O^+ respectively. For constant temperature these scale heights obey the simple relationships $H_1 = 4\sqrt{2}H_2 = 4H_3$. The quantity z_{traj} is a single-valued function of ρ determined by the trajectory of Cassini. From equation (6.2.3) it can be seen that if (ρ, z) is located on the trajectory of Cassini the two exponential summations cancel, leading to $n(\rho_{traj}, z_{traj}) = n_0(\rho_{traj})$, thereby recovering the electron density along the trajectory. In order to obtain a good fit to the lower cutoff we found that the scale height must vary as a function of the distance, ρ. We found that a scale height of $H_1 = 0.18$ gives a good fit to the left- hand branch of the lower cutoff (from about 0309 to 0330UT), but not the right-hand branch. Therefore, we set the scale height to a constant, H_0, along the left-hand branch. To fit the more variant right-hand branch the scale height was modeled as an inverse tangent function of ρ given by

$$H_1 = H_0 + A[\tan^{-1}(\frac{\rho - \rho_0}{l}) + \frac{\pi}{2}], \qquad (6.2.4)$$

where $H_0 = 0.18$, $A = \frac{2 - H_0}{2}$, $\rho_0 = 1.81$, and $l = 0.005$ were found to give the best overall fit. A plot of scale height H_1 with respect to ρ is shown in Figure 30. The scale heights H_2 and H_3 were calculated using $H_1 = 4\sqrt{2}H_2$ and $H_1 = 4H_3$.

Based on the electron density model described above and a simple dipole magnetic field, a two-dimensional ray tracing has been performed by carrying out a 4th order Runge-Kutta integration of the ray tracing equations assuming resonance cone propagation. It was found that the source position that gives the best fit is located almost exactly in the equatorial plane at a distance of 1.80 R_S from the center of Saturn. The computed low frequency cutoff is shown as the gray line in Figure 31. The fit is quite good at frequencies up to 4 kHz. At higher frequencies, the computed cutoff does not follow the dramatic rise of the plasma frequency after about 03:44UT. This sudden rise in frequency can not be explained by the present model, and is most likely due to some yet unknown aspect of the electron density distribution over the rings. Careful inspection shows that this high frequency emission region is very close to the inner edge of Cassini division, which is located at 1.95 R_s. The free passage of plasma through the rings in the Cassini division most likely causes major changes in the electron density distribution that are not adequately represented in our model.

6.3 Discussion

Since auroral hiss is produced by electron beams, an emission source at the equator implies that there are electron beams directed outward, along the magnetic field lines away from the rings. The computed source position ($\rho = 1.80R_S$) is very close to Saturn's synchronous orbit point ($\rho_S = 1.86R_S$). It therefore implies that there are electron beams directing upward from the equator near the synchronous orbit point. Figure 32 demonstrates a possible electron beam generation process near the synchronous orbit point. The drag force of the rings acting on the plasma induces an inward directed current inside of the synchronous point and an outward directed current outside of the synchronous point. Such a current could be produced by either pick-up ions produced by an ionization process near the ring plane or by the co-rotational electric field and a Pedersen conductivity. Continuity of current in the ring plane then implies that there must be field-aligned currents flowing inward toward the ring plane. These field-aligned currents are most likely carried by electron beams directed away from equator. The auroral hiss emission observed by Cassini would be then produced by these electron beams.

VII. CONCLUSIONS

By studying the auroral hiss observed in the magnetosphere of the Earth, Jupiter and Saturn, we have shown that auroral hiss is a universal wave phenomenon that can occur at any planet with a magnetic field. The funnel-shaped spectrum of auroral hiss can be explained by whistler-mode propagation near the resonance cone. Assuming that the auroral hiss propagates near the resonance cone, ray tracing can be used to determine where the auroral hiss is produced. Since it is believed that auroral hiss is generated by low energy electron beams the occurrence of the auroral hiss always indicate the existence of electron beams. Therefore the study of auroral hiss can provide important information on the electron acceleration processes in the magnetospheres of the planets.

Figure 1. Frequency-time spectrograms of auroral hiss observed by the Injun 5 satellite. The red and green colors represent upward and downward propagation, respectively.

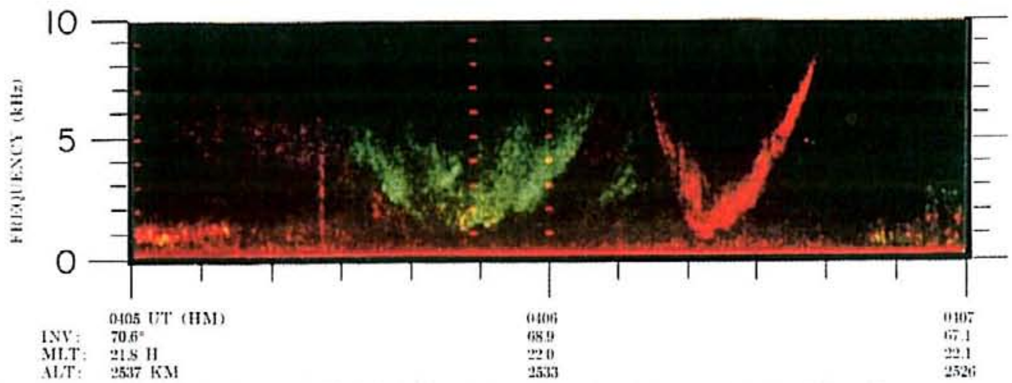
10
5
0
FREQUENCY (kHz)
0405 UT (HM)
INV: 70.6°
MLT: 21.8 H
ALT: 2537 KM
0406
68.9
22.0
2533
0407
67.1
22.1
2526

Plate 4.

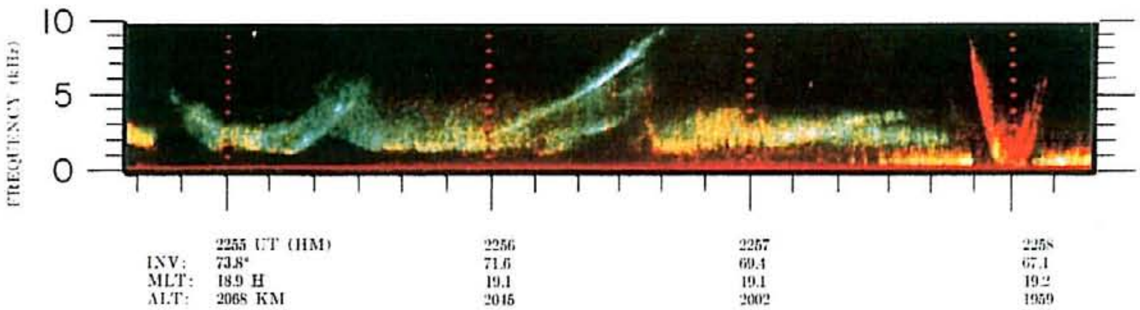
10
5
0
FREQUENCY (kHz)
2255 UT (HM)
INV: 73.8°
MLT: 18.9 H
ALT: 2068 KM
2256
71.6
19.1
2045
2257
69.4
19.1
2002
2258
67.1
19.2
1959

Figure 2. Spectrogram of auroral hiss observed by DE 1 spacecraft. The asymmetric funnel-shaped low frequency cutoff is clearly shown.

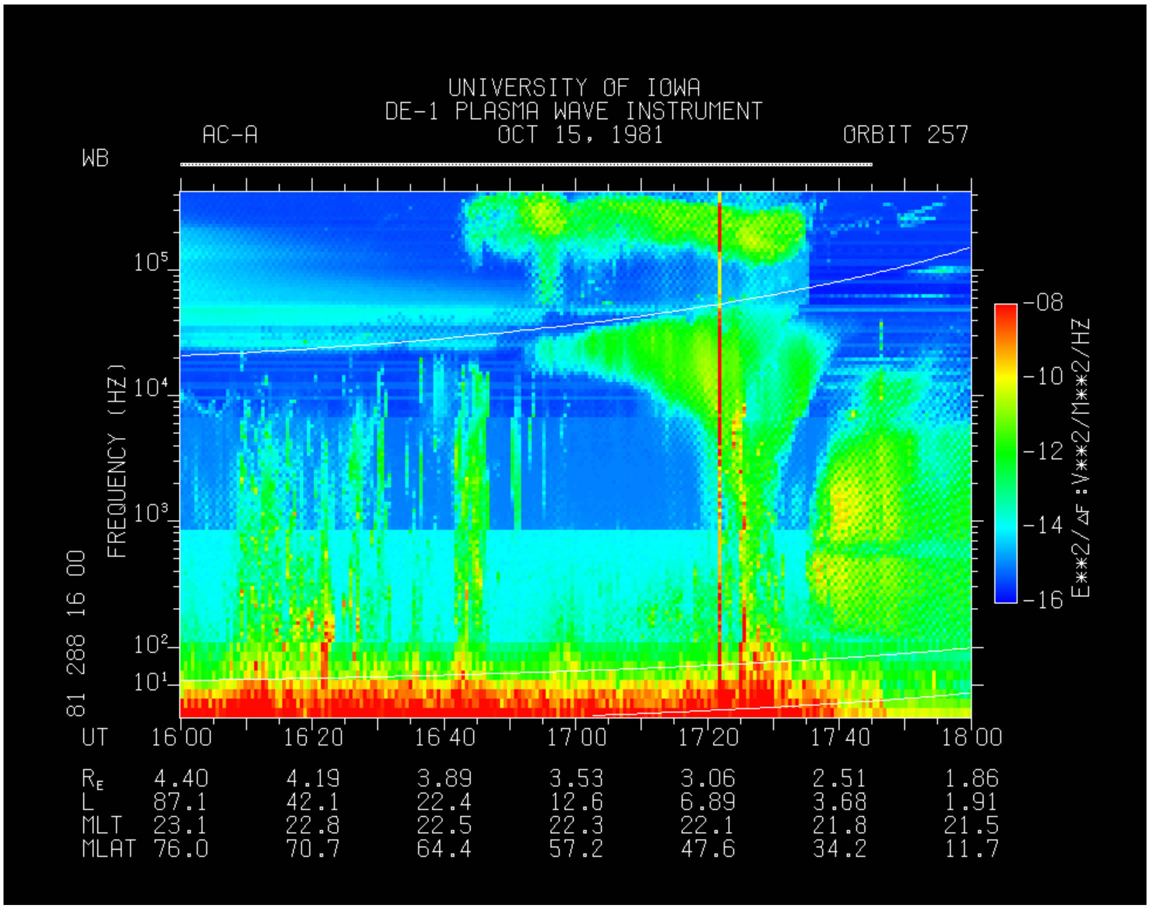

UNIVERSITY OF IOWA
DE-1 PLASMA WAVE INSTRUMENT
AC-A
OCT 15, 1981
ORBIT 257
WB
FREQUENCY (HZ)
81 288 16 00
E**2/ΔF:V**2/M**2/HZ
-08
-10
-12
-14
-16
UT 16 00 16 20 16 40 17 00 17 20 17 40 18 00
RE 4.40 4.19 3.89 3.53 3.06 2.51 1.86
L 87.1 42.1 22.4 12.6 6.89 3.68 1.91
MLT 23.1 22.8 22.5 22.3 22.1 21.8 21.5
MLAT 76.0 70.7 64.4 57.2 47.6 34.2 11.7

Figure 3. Auroral hiss produced by artificial electron beams with energy 1 keV. The clear funnel-shaped low frequency cutoff on both sides is clearly distinguishable.

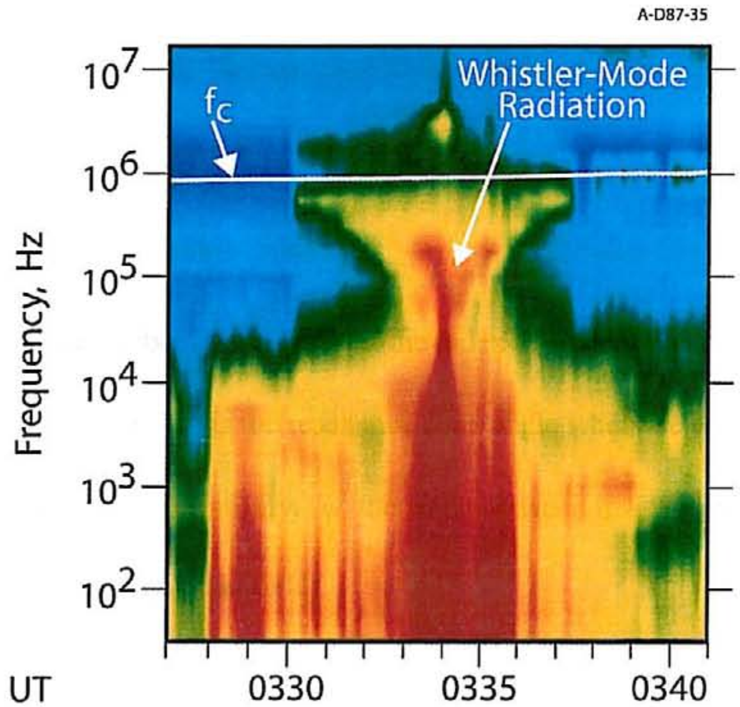

PDP, Day 213, August 1, 1985

Figure 4. Polar plots of the surface of the index of refraction with frequencies f_1, f_2 and f_3. ($\theta_{\mathrm{Re}s}$ is the resonance cone angle when the index of refraction $n(\theta)$ goes to infinity. ψ the angle between limiting ray path direction and the magnetic field).

A-D02-104a

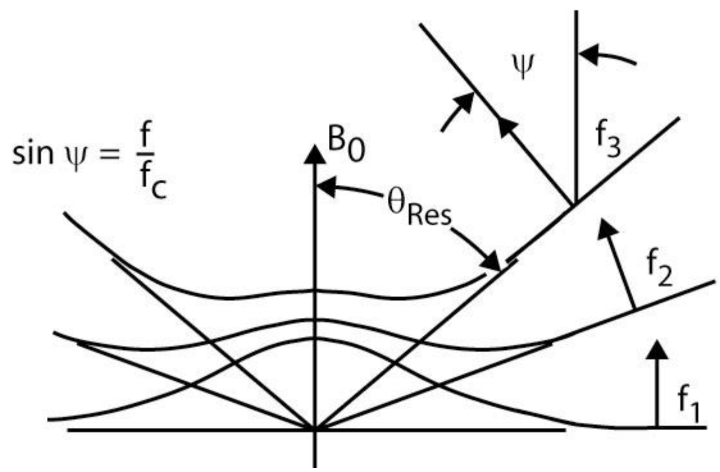

Figure 5. Funnel-shaped low frequency cutoff calculated from whistler-mode propagation near resonance cone.

A-D82-68-3

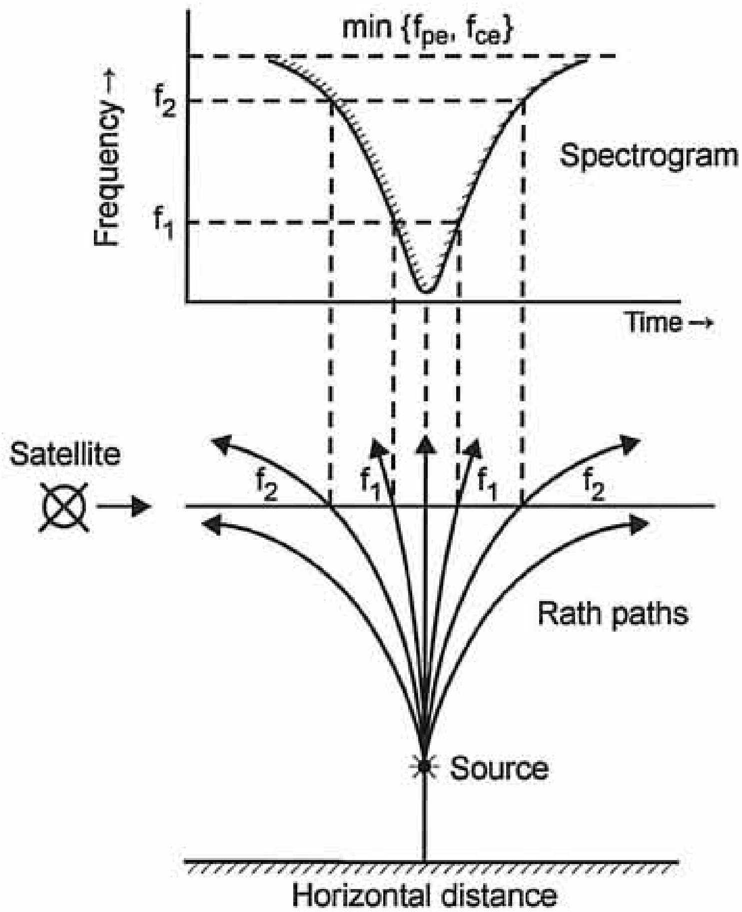
min {f_pe, f_ce}
Frequency →
f2
f1
Spectrogram
Time →
Satellite
f2
f1
f1
f2
Rath paths
Source
Horizontal distance

Figure 6. Electric field spectrum for a specific universal time from an auroral hiss event observed by Cassini spacecraft on July 1, 2004. The vertical line representing the dramatic rise of the intensity of the emission infers a cutoff frequency.

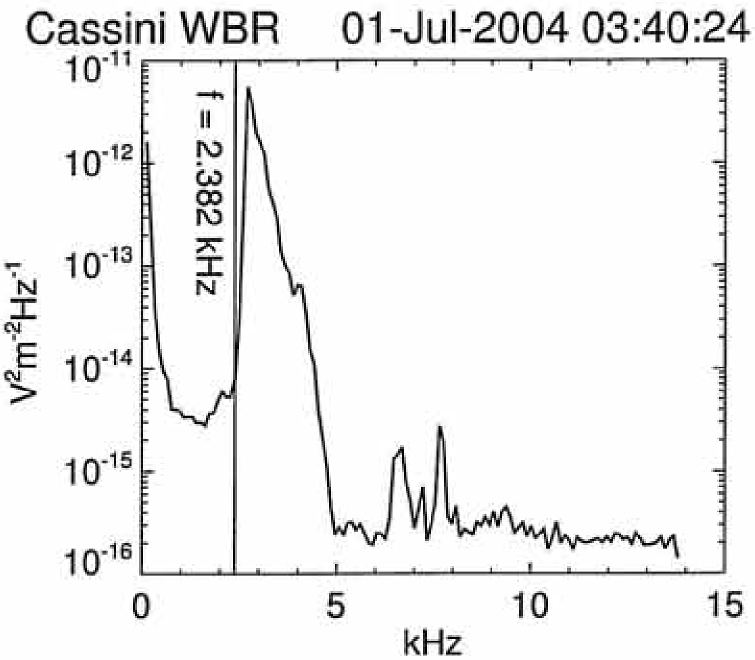
Cassini WBR 01-Jul-2004 03:40:24
f = 2.382 kHz
$V^2m^{-2}Hz^{-1}$
10^{-11}
10^{-12}
10^{-13}
10^{-14}
10^{-15}
10^{-16}
0
5
10
15
kHz

Figure 7. Illustration of a dipolar magnetic-field line and various geomagnetic parameters.

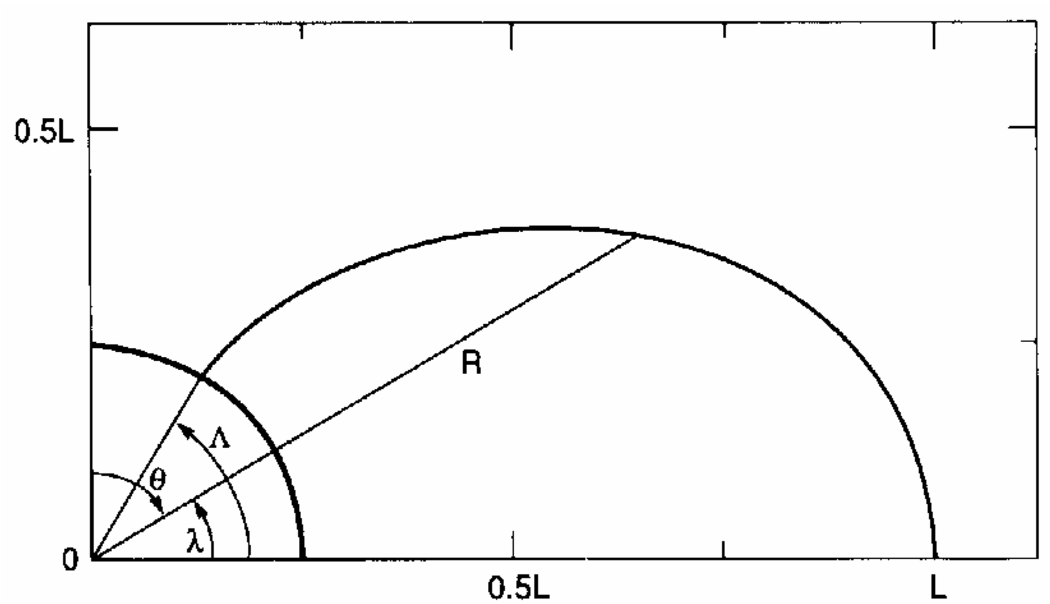
0.5L
R
Λ
θ
λ
0
0.5L
L

Figure 8. Demonstration of two-dimensional ray path tracing. P_0 is a point on the trajectory. P_1 is obtained by traced back along ψ_{Res}, the angle between the magnetic field and the ray path.

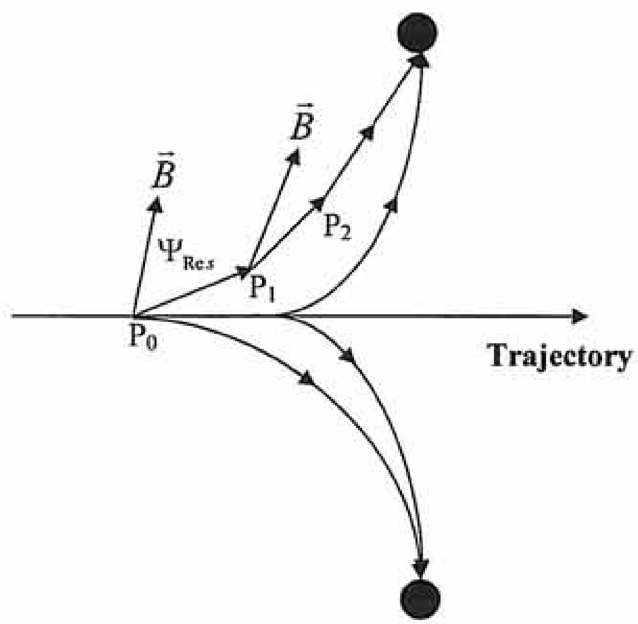
$\vec{B}$
$\vec{B}$
Ψ_{Res}
P_2
P_1
P_0
Trajectory

Figure 9. Pairs of auroral hiss events detected by the Polar satellite on August 27th, 1996. The two events are separated by a time interval of about 20 minutes.

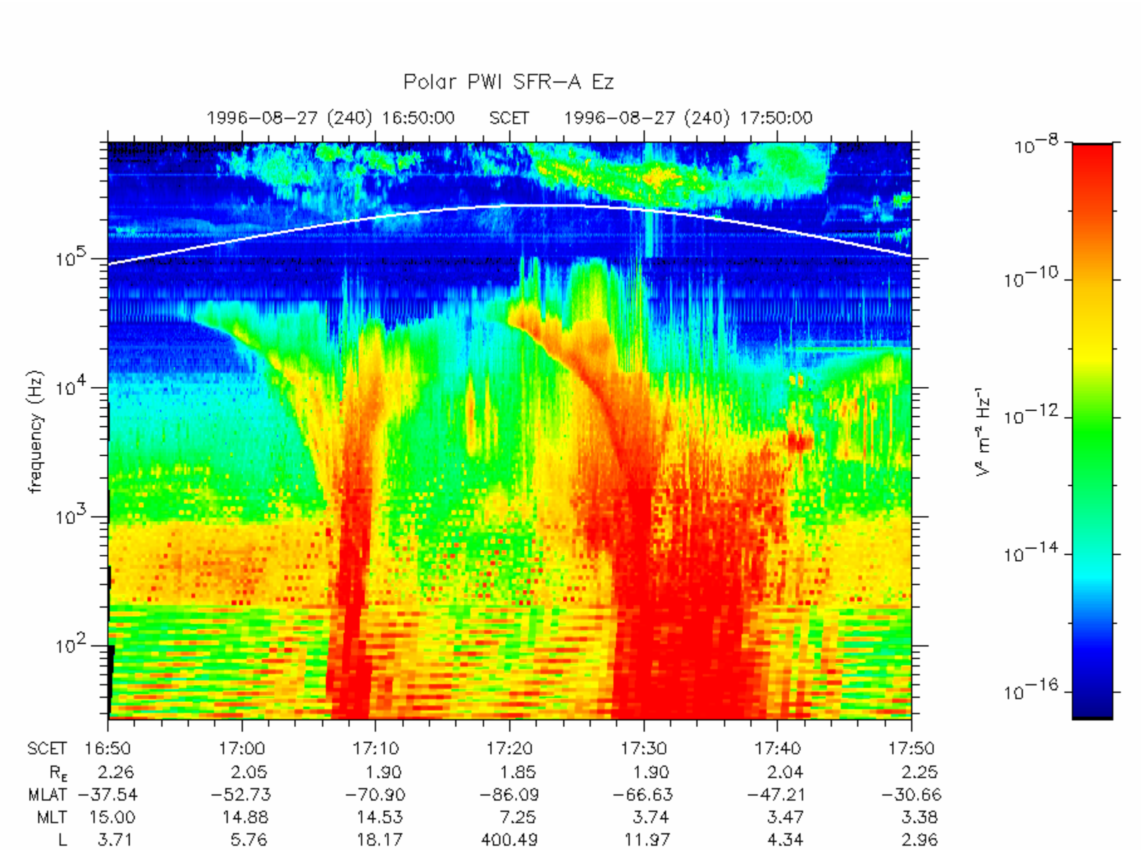

Polar PWI SFR–A Ez
1996–08–27 (240) 16:50:00 SCET 1996–08–27 (240) 17:50:00
frequency (Hz)
V² m⁻² Hz⁻¹
SCET 16:50 17:00 17:10 17:20 17:30 17:40 17:50
RE 2.26 2.05 1.90 1.85 1.90 2.04 2.25
MLAT −37.54 −52.73 −70.90 −86.09 −66.63 −47.21 −30.66
MLT 15.00 14.88 14.53 7.25 3.74 3.47 3.38
L 3.71 5.76 18.17 400.49 11.97 4.34 2.96

Figure 10. A series of ray paths computed for two source positions which produced a good fit to the funnel-shaped auroral hiss pair observed by Polar near the south pole of the Earth.

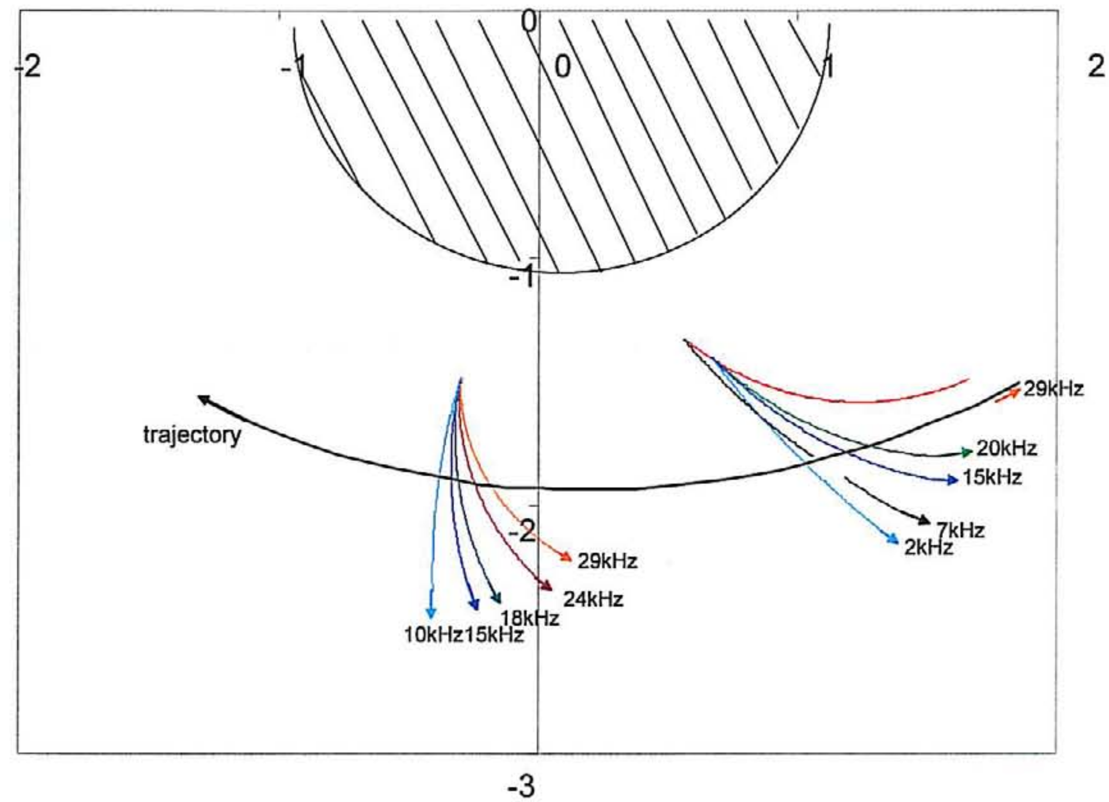
0
-2
-1
0
1
2
-1
-2
-3
trajectory
29kHz
20kHz
15kHz
7kHz
2kHz
29kHz
24kHz
18kHz
10kHz
15kHz

Figure 11. The trajectory of Galileo during the Io 32 flyby.

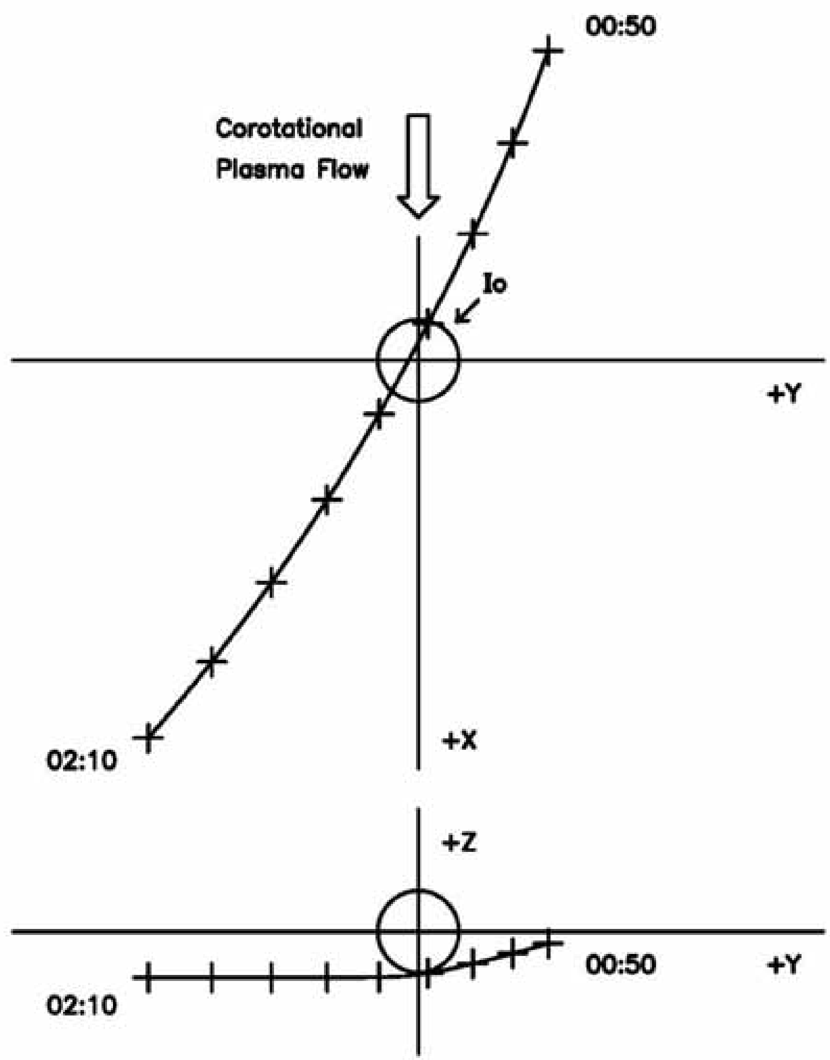
00:50
Corotational
Plasma Flow
Io
+Y
02:10
+X
+Z
00:50
+Y
02:10

Figure 12. Auroral hiss observed by Galileo near the south pole of Jupiter's moon Io.

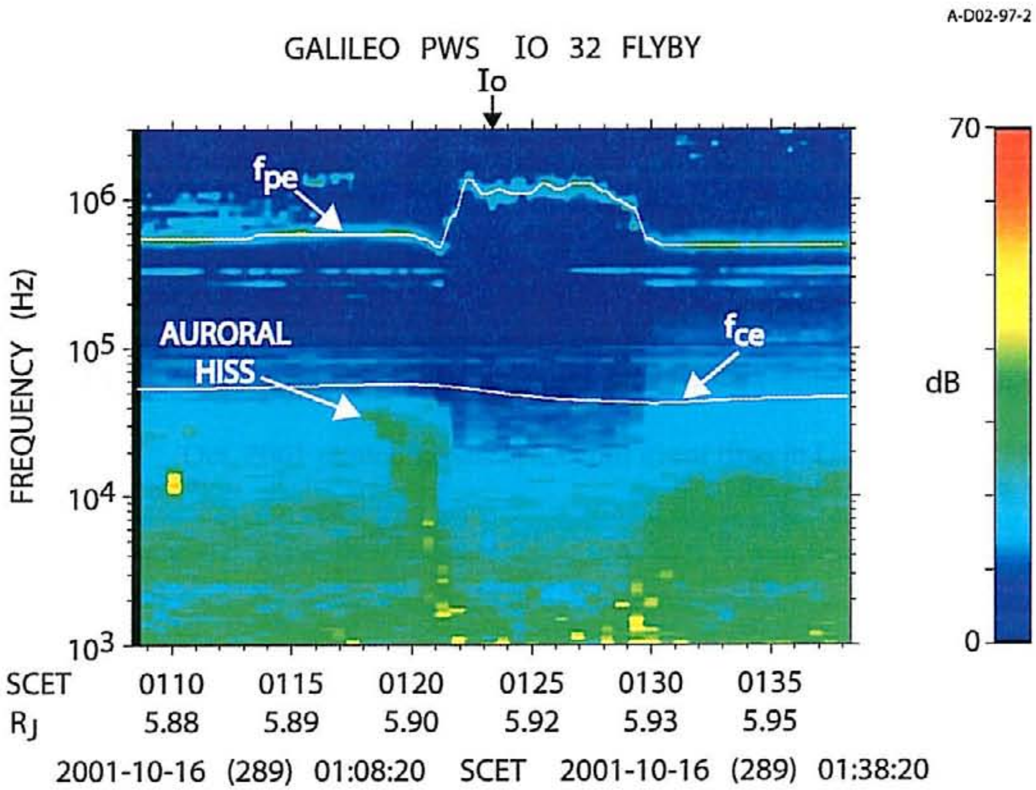
A-D02-97-2
GALILEO PWS IO 32 FLYBY
Io
fpe
fce
AURORAL
HISS
FREQUENCY (Hz)
10^6
10^5
10^4
10^3
70
dB
0
SCET 0110 0115 0120 0125 0130 0135
RJ 5.88 5.89 5.90 5.92 5.93 5.95
2001-10-16 (289) 01:08:20 SCET 2001-10-16 (289) 01:38:20

Figure 13. Magnetic field components measured by the Galileo Magnetometer on 16 Oct. 2001 plotted versus spacecraft event time in UT.

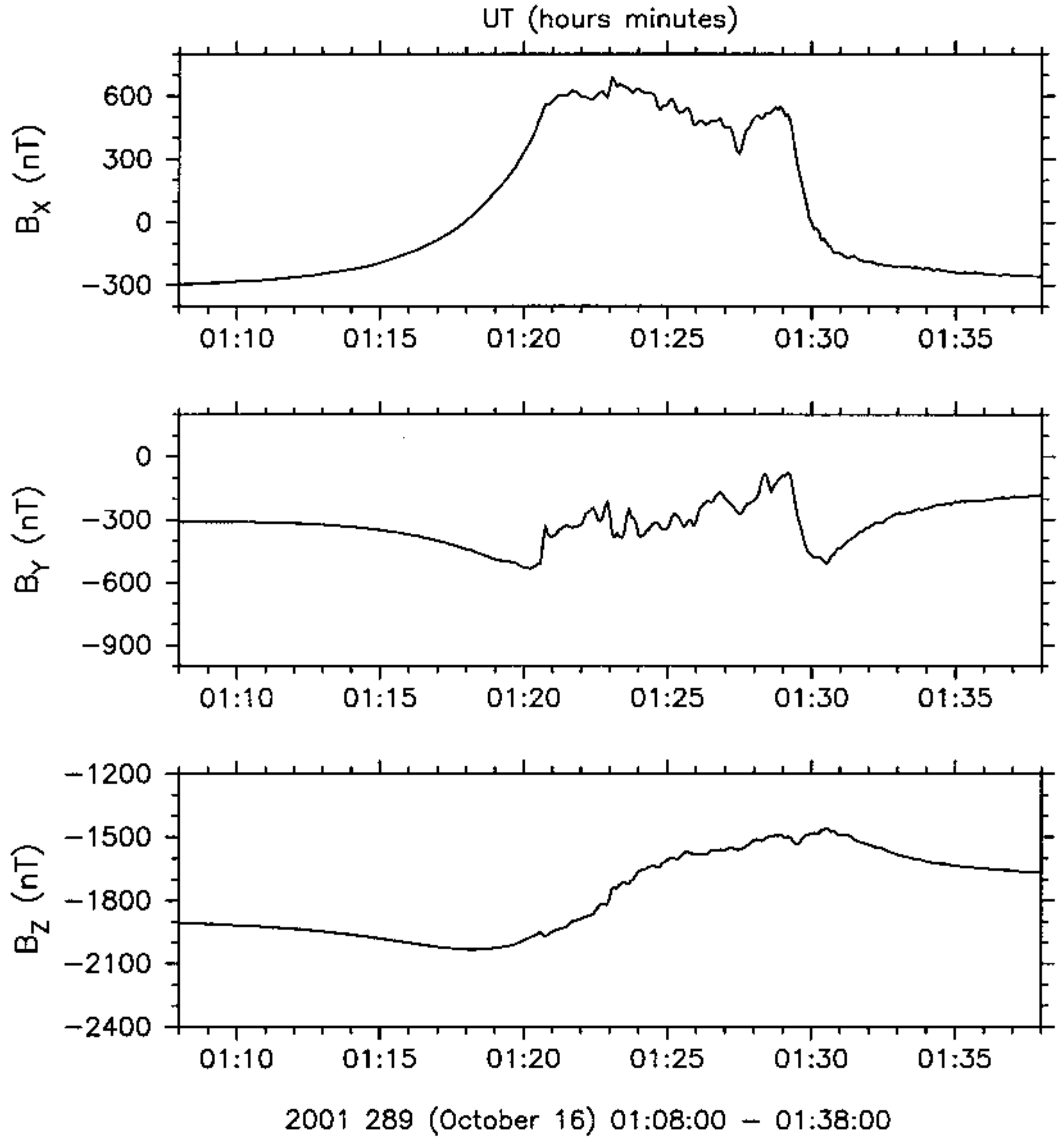
UT (hours minutes)
B_X (nT)
600
300
0
−300
01:10
01:15
01:20
01:25
01:30
01:35
B_Y (nT)
0
−300
−600
−900
B_Z (nT)
−1200
−1500
−1800
−2100
−2400
2001 289 (October 16) 01:08:00 – 01:38:00

Figure 14. Dependence of Jupiter’s decametric radio emission on the position of Io.

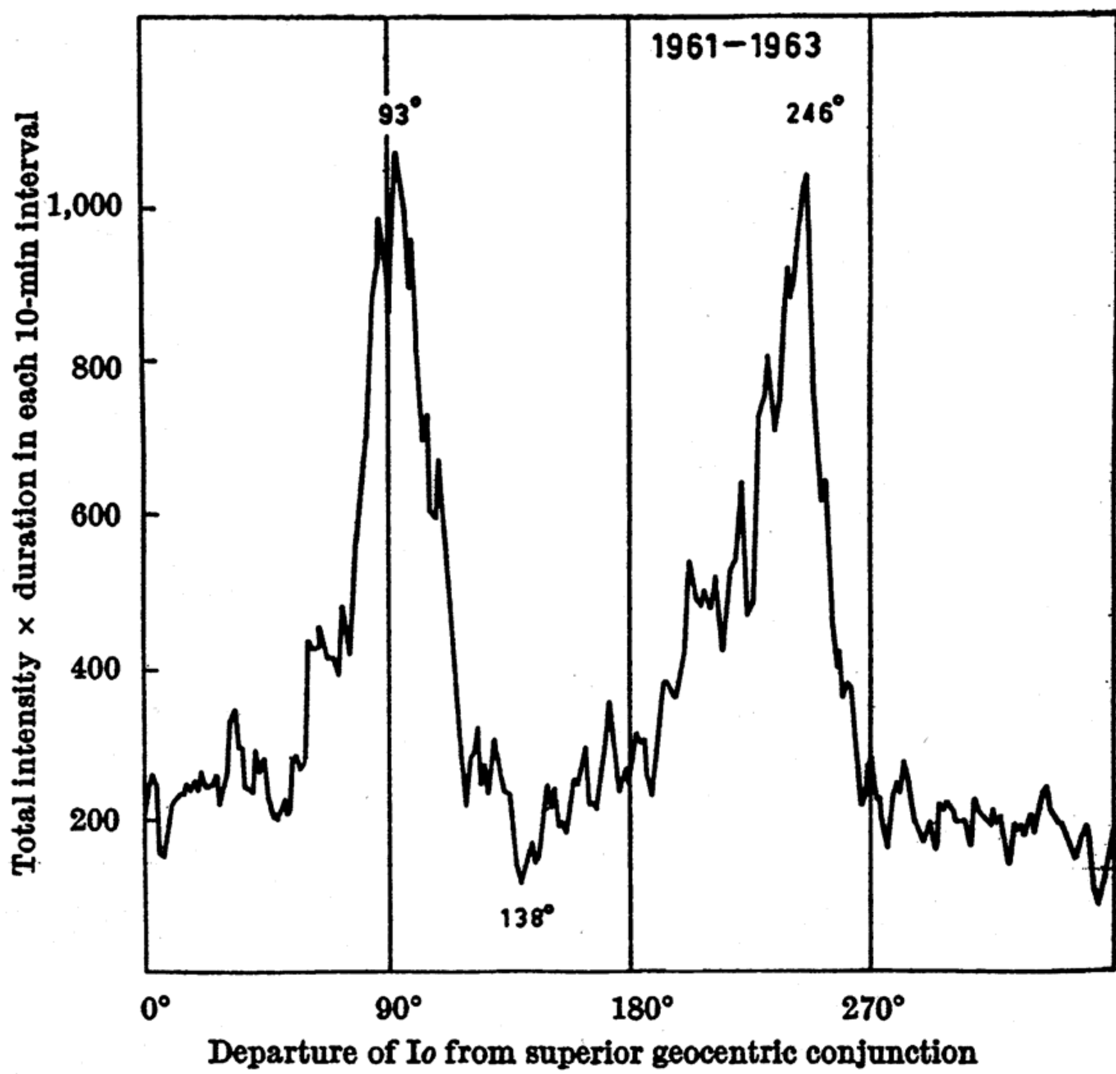
1961—1963
93°
246°
138°
1,000
800
600
400
200
Total intensity × duration in each 10-min interval
0°
90°
180°
270°
Departure of Io from superior geocentric conjunction

Figure 15. Meridian plane view of the current circuit of Io and Jupiter. Also the trajectory of Galileo is shown (not to scale).

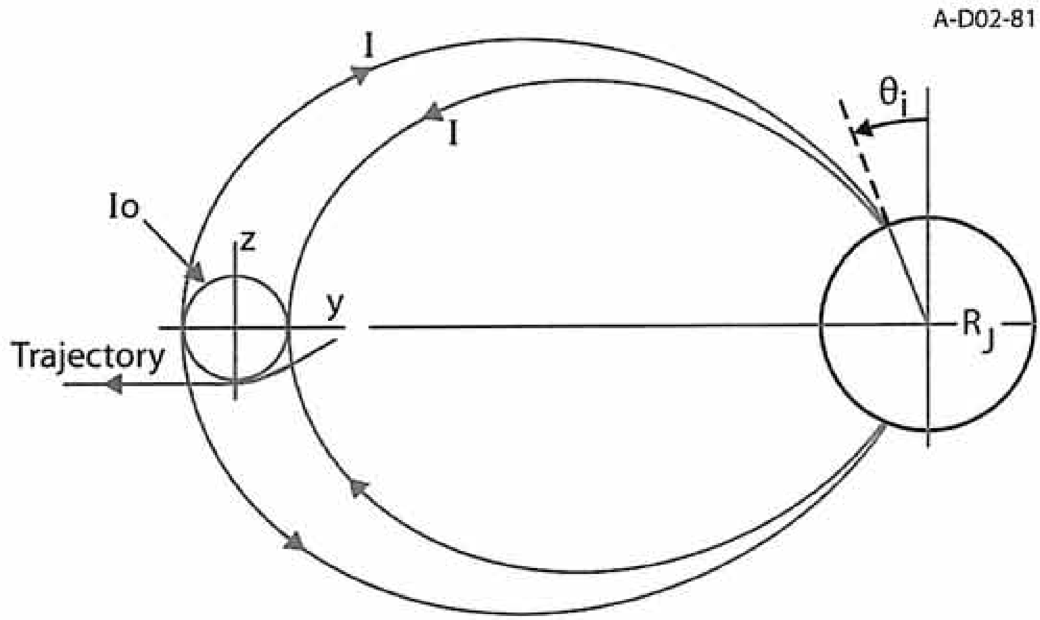
A-D02-81
I
I
θ_i
Io
z
y
Trajectory
R_J

Figure 16. Comparison of the observed perturbation magnetic field components and best-fit magnetic fields for twin oppositely directed currents and for a line current.

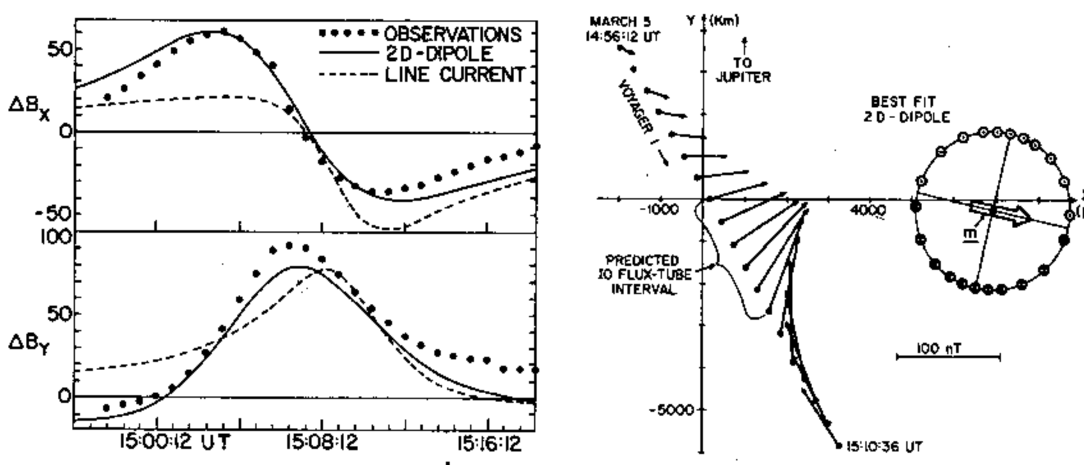

OBSERVATIONS
2D-DIPOLE
LINE CURRENT
ΔB_X
ΔB_Y
50
0
-50
100
15:00:12 UT
15:08:12
15:16:12
MARCH 5
14:56:12 UT
Y (Km)
TO JUPITER
VOYAGER I
BEST FIT
2 D - DIPOLE
X (km)
-1000
4000
-5000
m
PREDICTED
IO FLUX-TUBE
INTERVAL
100 nT
15:10:36 UT

Figure 17. Three-dimensional sketch of ‘Alfven wings’ generated by an ideal conductor in a collisionless plasma.

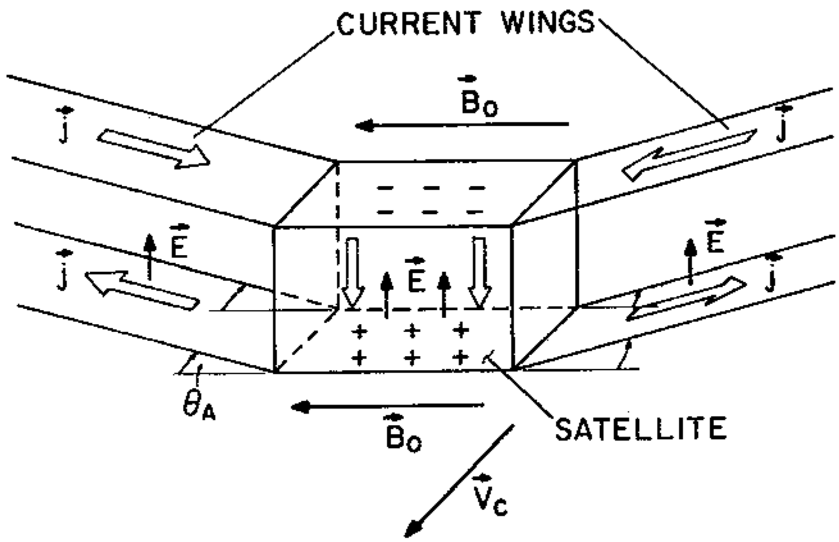
CURRENT WINGS
$\vec{B}_0$
$\vec{j}$
$\vec{j}$
$\vec{E}$
$\vec{j}$
$\vec{E}$
$\vec{E}$
$\vec{j}$
θ_A
$\vec{B}_0$
SATELLITE
$\vec{V}_c$

Figure 18. Demonstration of the geometric relation for locating the point source position when using best-fit propagation cutoff.

A-D02-96

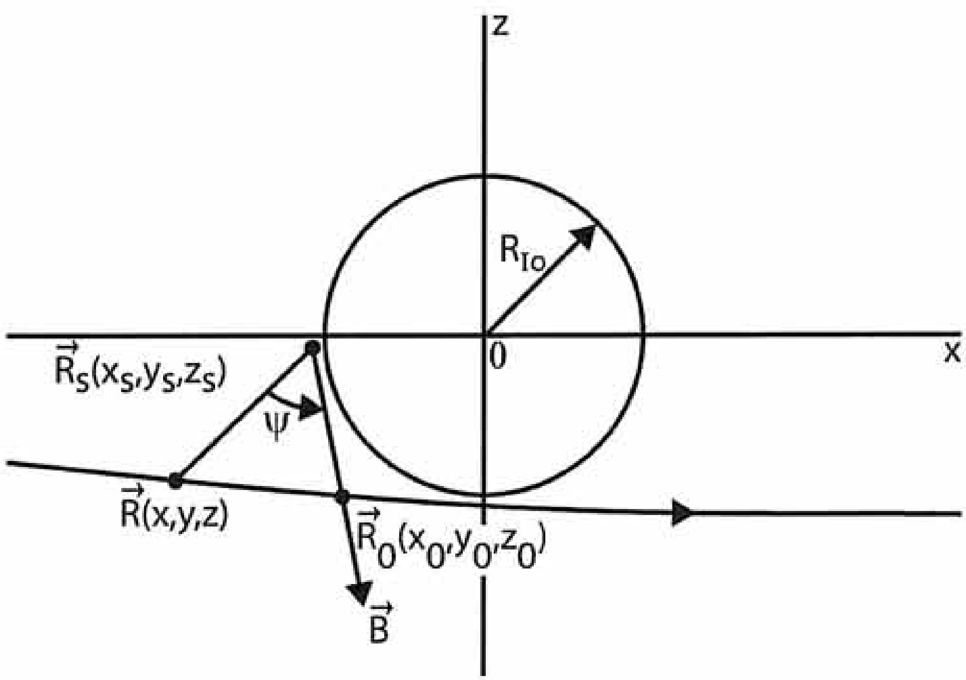

Figure 19. Fitting curves for three different point source positions. The solid circles are sampled from the cutoff emission boundary of the spectrum; three fitting curves are calculated for three different source positions.

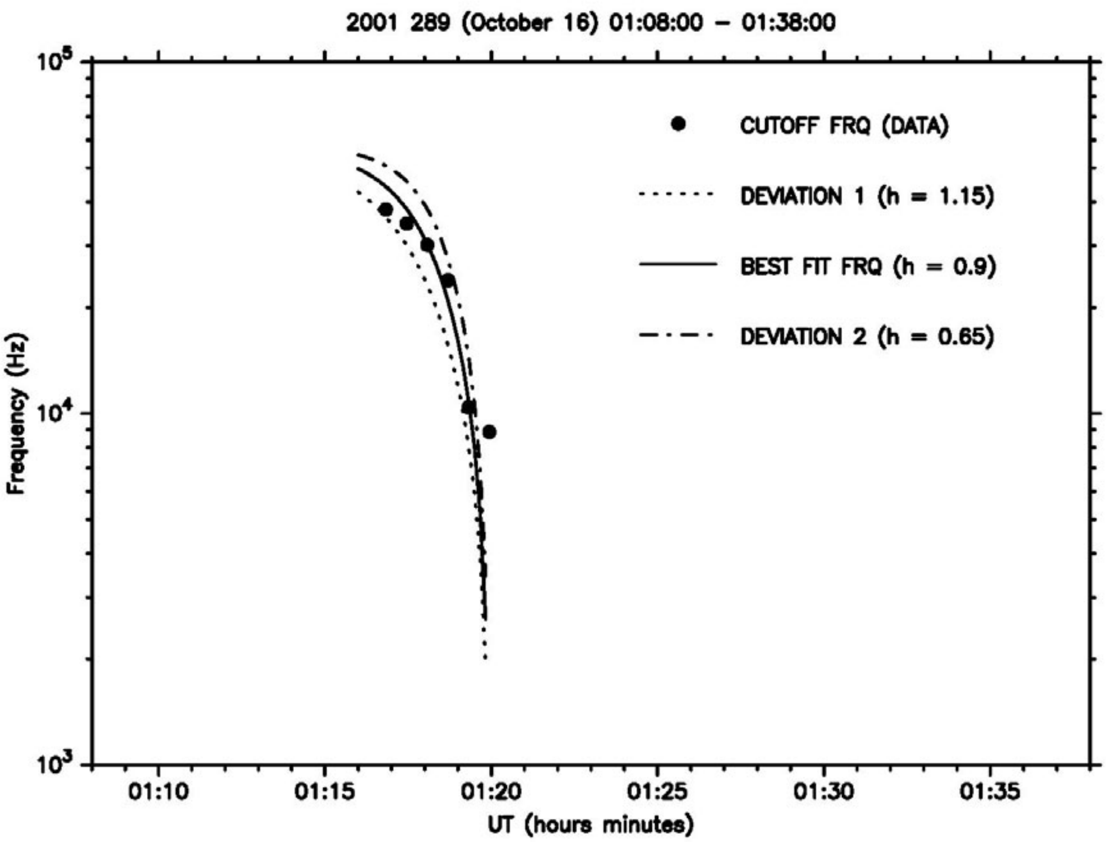
2001 289 (October 16) 01:08:00 – 01:38:00
CUTOFF FRQ (DATA)
DEVIATION 1 (h = 1.15)
BEST FIT FRQ (h = 0.9)
DEVIATION 2 (h = 0.65)
Frequency (Hz)
10^5
10^4
10^3
01:10
01:15
01:20
01:25
01:30
01:35
UT (hours minutes)

Figure 20. The best-fit curve for a point source is plotted on the spectrum for the auroral hiss event observed by Galileo on Oct. 16th, 1996.

A-D02-105

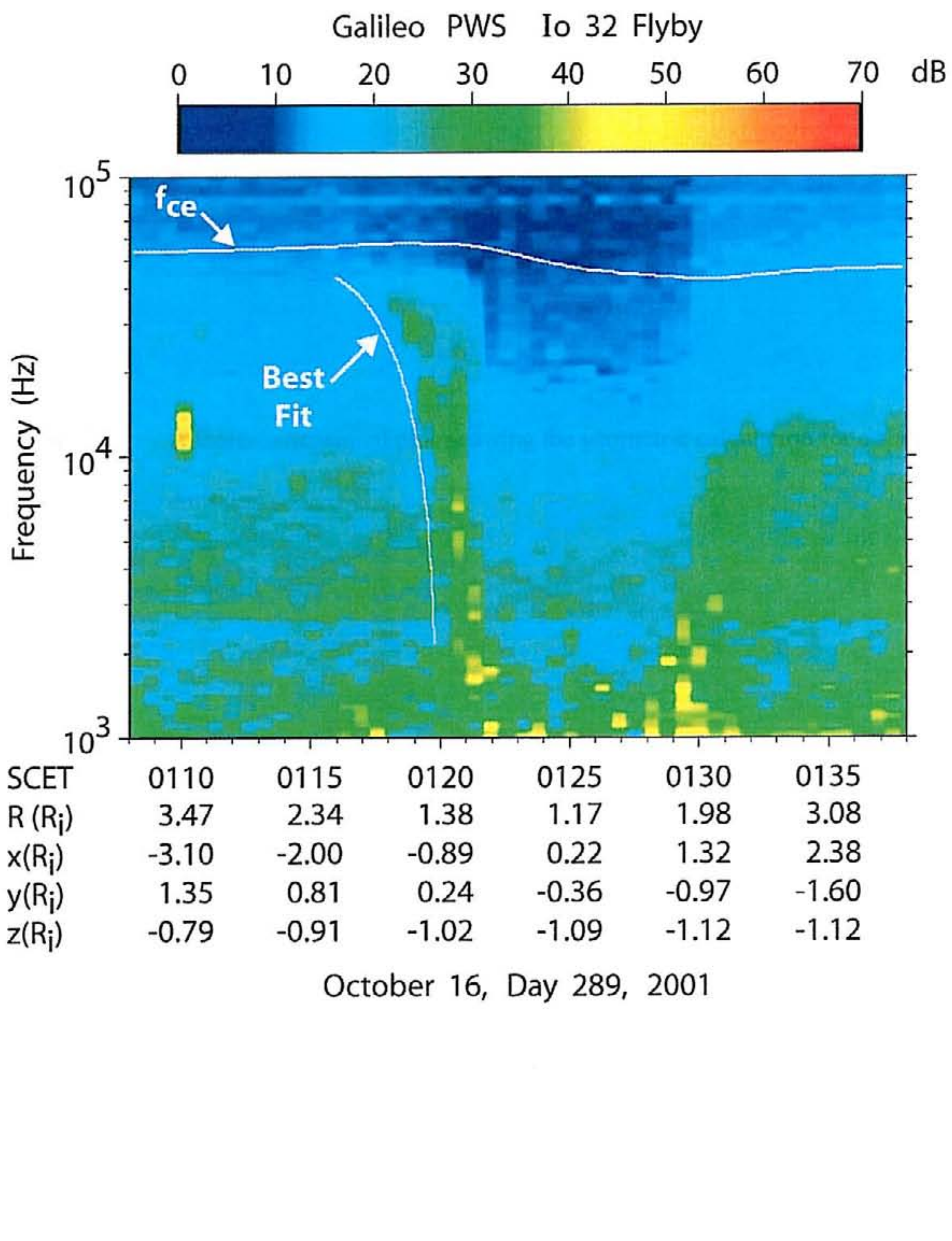
Galileo PWS Io 32 Flyby
0 10 20 30 40 50 60 70 dB
10^5
f_{ce}
Best Fit
Frequency (Hz)
10^4
10^3
SCET 0110 0115 0120 0125 0130 0135
R (R_j) 3.47 2.34 1.38 1.17 1.98 3.08
x(R_j) -3.10 -2.00 -0.89 0.22 1.32 2.38
y(R_j) 1.35 0.81 0.24 -0.36 -0.97 -1.60
z(R_j) -0.79 -0.91 -1.02 -1.09 -1.12 -1.12
October 16, Day 289, 2001

Figure 21. A three-dimensional plot showing the geometric calculation for a sheet emission source.

A-D02-83

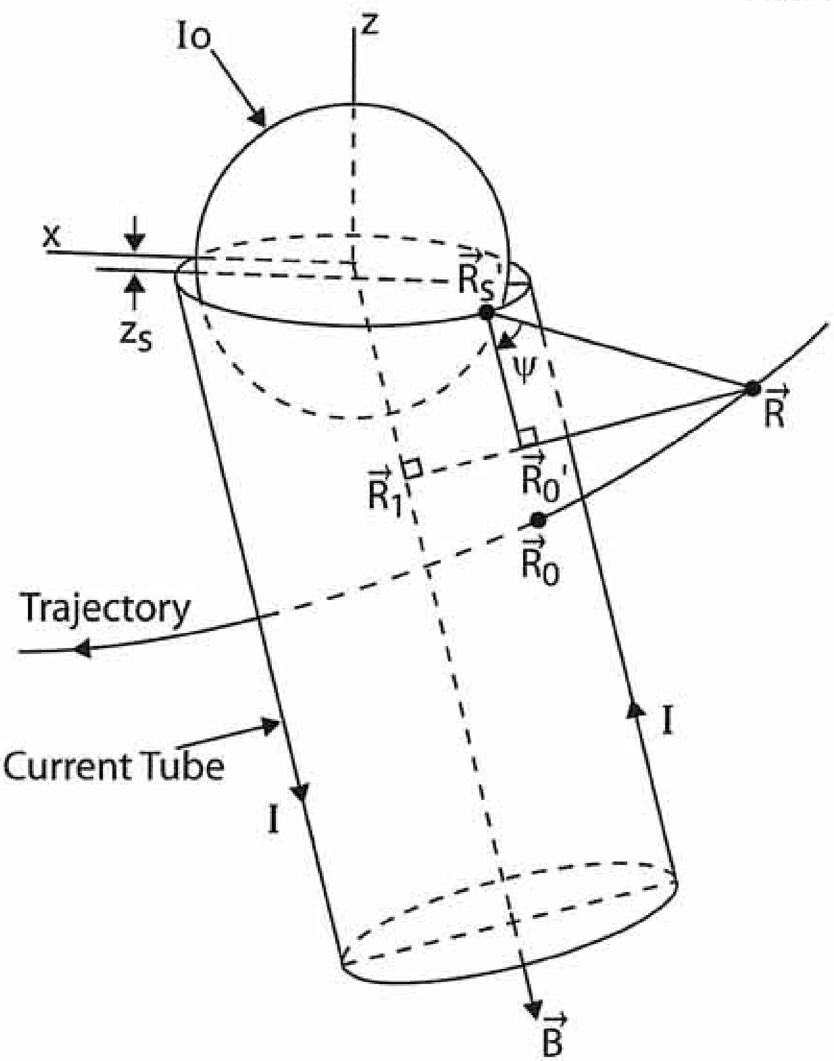

Io
z
x
z_s
$\vec{R}_s'$
ψ
$\vec{R}$
$\vec{R}_1$
$\vec{R}_0'$
$\vec{R}_0$
Trajectory
Current Tube
I
I
$\vec{B}$

Figure 22. Cutoff frequency calculated from a sheet emission source (solid line) vs. the sampled cutoff data (solid circles).

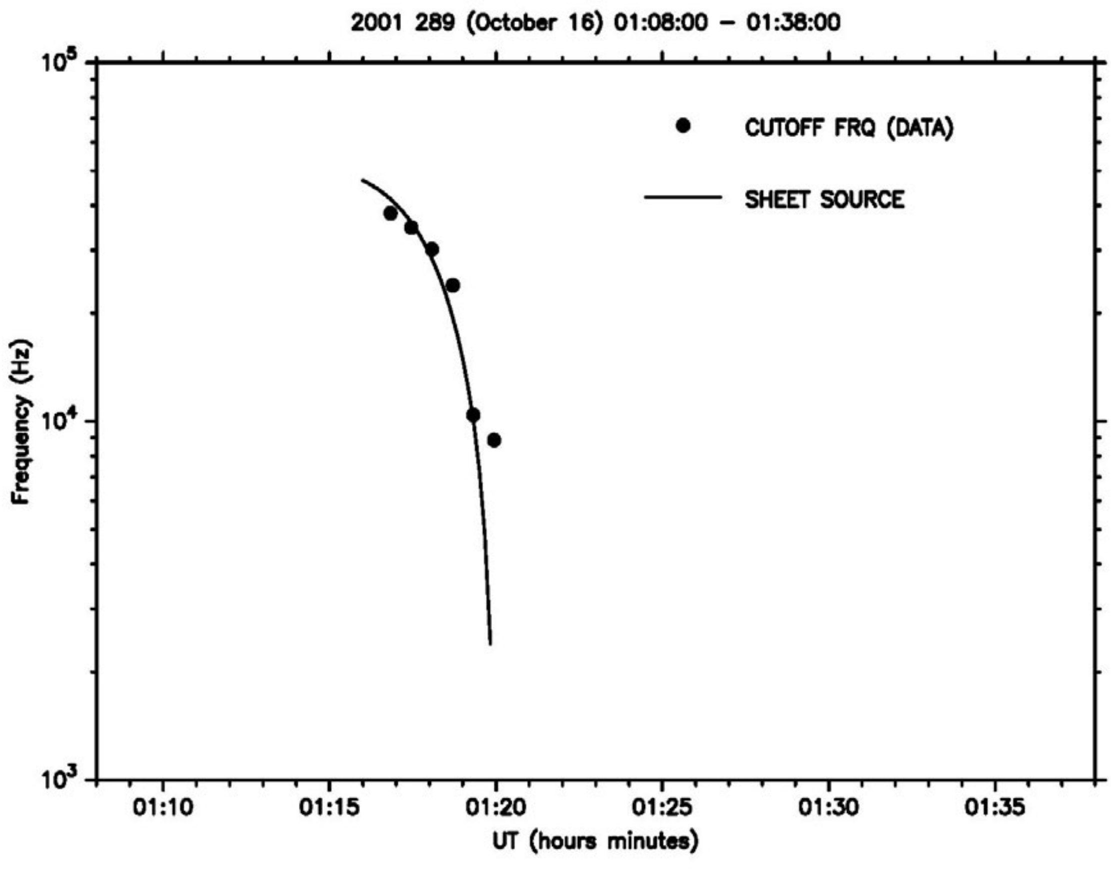
2001 289 (October 16) 01:08:00 – 01:38:00
CUTOFF FRQ (DATA)
SHEET SOURCE
Frequency (Hz)
UT (hours minutes)
10^5
10^4
10^3
01:10
01:15
01:20
01:25
01:30
01:35

Figure 23. Auroral hiss observed by Galileo in the Io torus on Nov. 5^{th}, 2002.

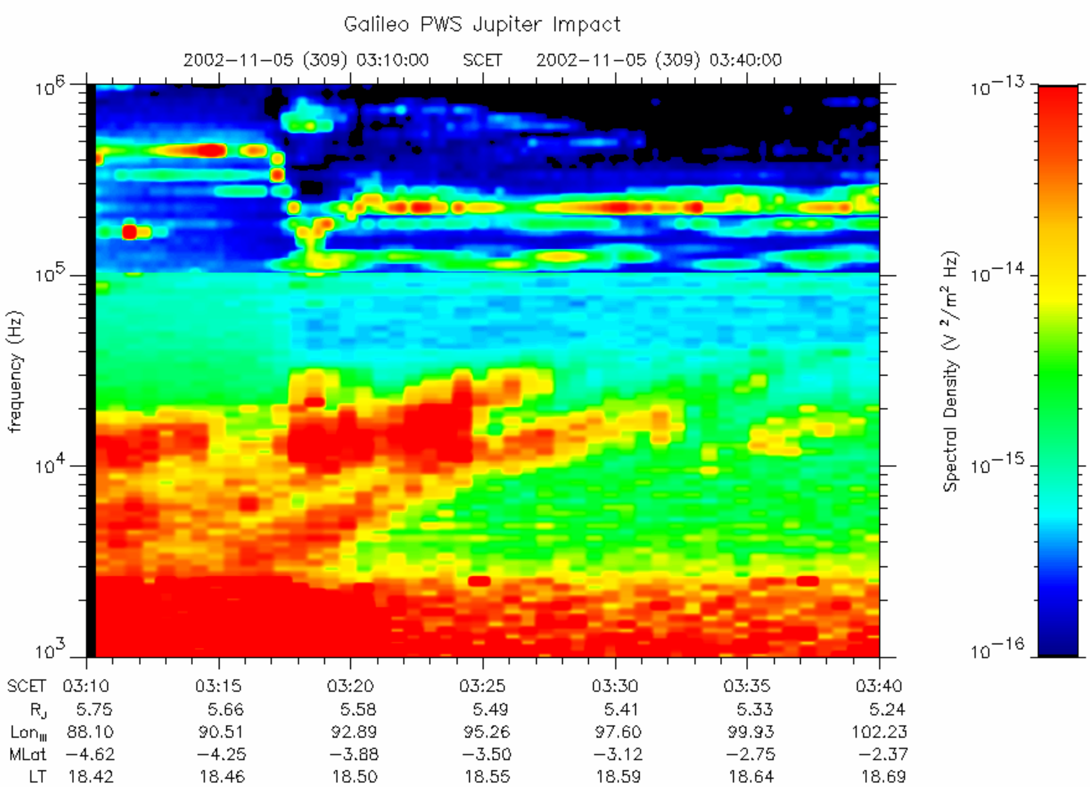

Galileo PWS Jupiter Impact
2002-11-05 (309) 03:10:00 SCET 2002-11-05 (309) 03:40:00
frequency (Hz)
Spectral Density (V ²/m² Hz)
SCET 03:10 03:15 03:20 03:25 03:30 03:35 03:40
R_J 5.75 5.66 5.58 5.49 5.41 5.33 5.24
Lon_III 88.10 90.51 92.89 95.26 97.60 99.93 102.23
MLat −4.62 −4.25 −3.88 −3.50 −3.12 −2.75 −2.37
LT 18.42 18.46 18.50 18.55 18.59 18.64 18.69

Figure 24. Ray path tracing for auroral hiss event observed by Galileo near Jupiter's Io torus on Nov. 5th, 2002. The ray paths of various frequencies converge to two possible sources, one north and the other south of the spacecraft.

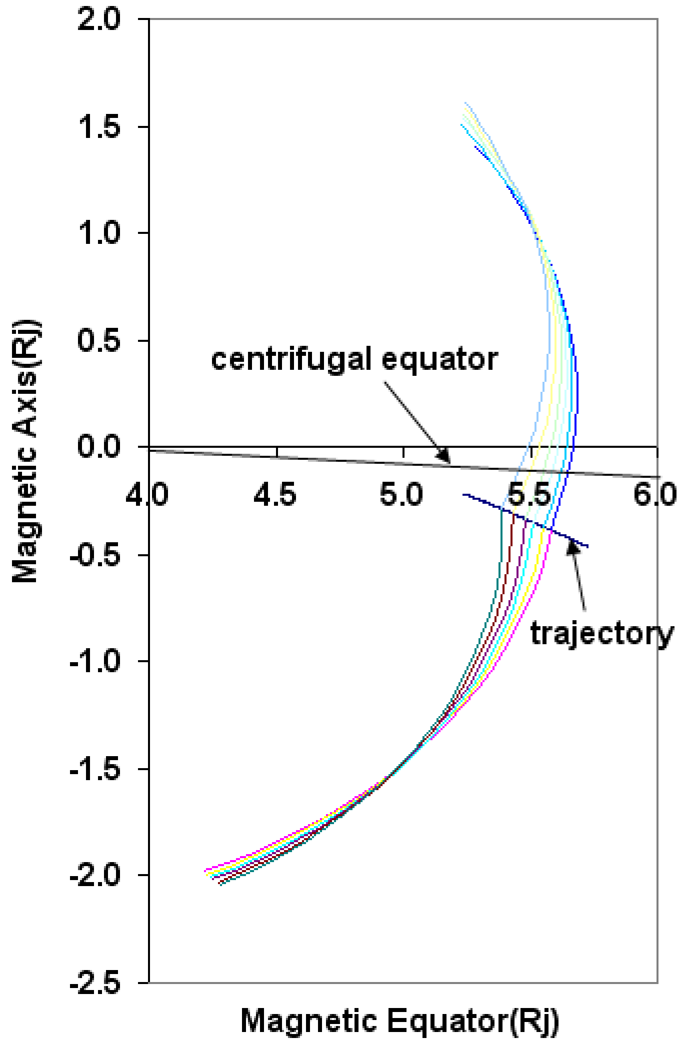
2.0
1.5
1.0
0.5
0.0
-0.5
-1.0
-1.5
-2.0
-2.5
4.0
4.5
5.0
5.5
6.0
centrifugal equator
trajectory
Magnetic Axis(Rj)
Magnetic Equator(Rj)

Figure 25. Two possible source positions (represented by stars) superimposed on a density contour of the Io torus based on the centrifugal symmetry surface. Superimposed on the contours in purple is the Galileo J0 trajectory.

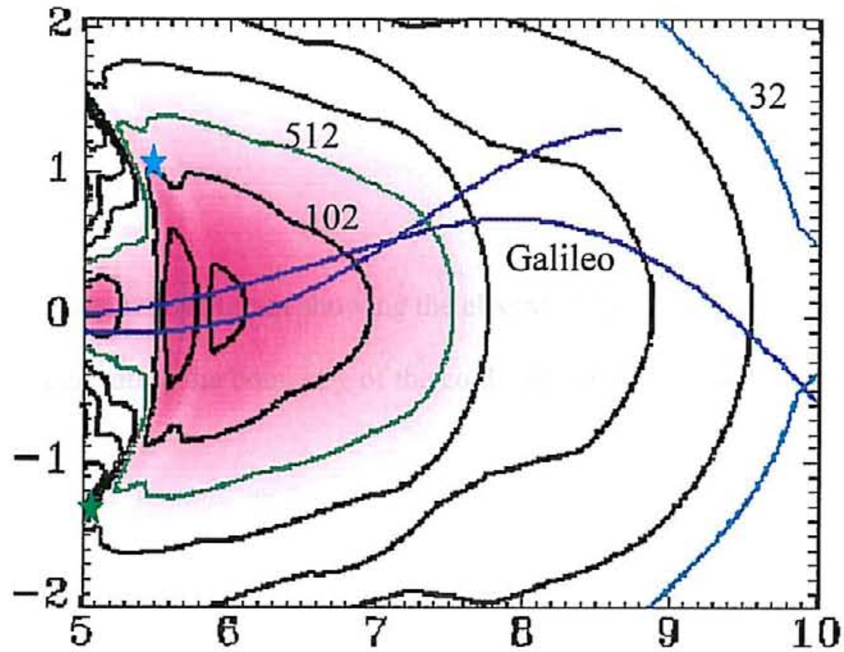
512
102
32
Galileo
2
1
0
−1
−2
5
6
7
8
9
10

Figure 26. Schematic diagram showing the electron beams and the field-aligned current on the boundary of the cold and hot plasma of the torus.

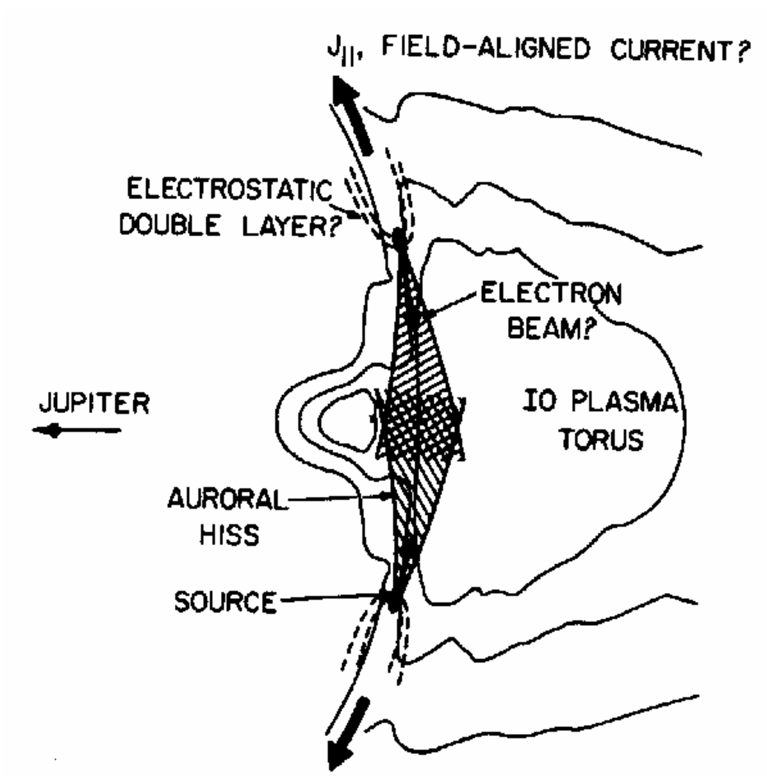
$J_{||}$, FIELD-ALIGNED CURRENT?
ELECTROSTATIC
DOUBLE LAYER?
ELECTRON
BEAM?
JUPITER
IO PLASMA
TORUS
AURORAL
HISS
SOURCE

Figure 27. Funnel-shaped auroral hiss emissions observed by the Cassini spacecraft during its first pass of Saturn's rings on July 1, 2004.

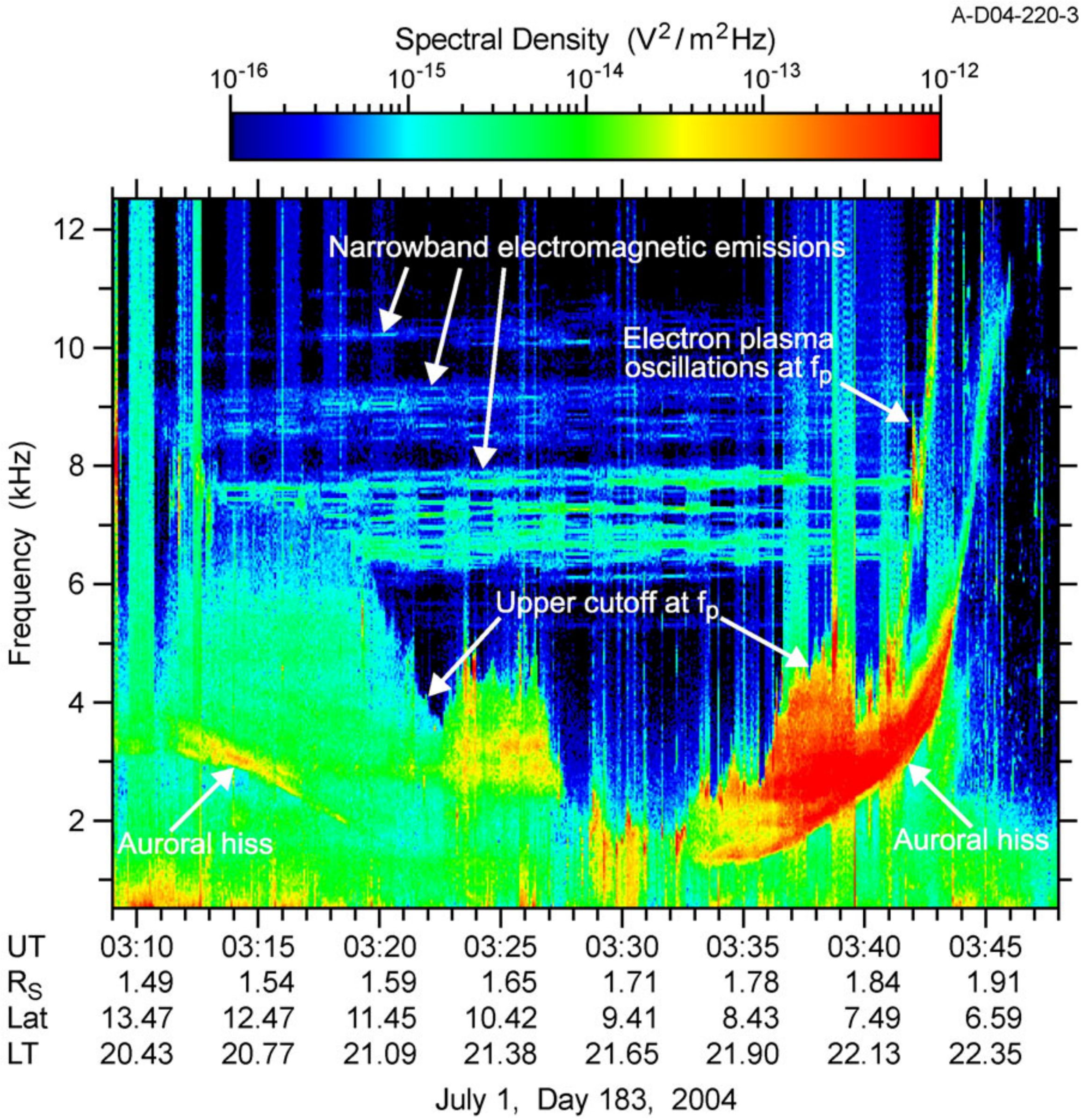
A-D04-220-3
Spectral Density (V^2/m^2Hz)
10^{-16} 10^{-15} 10^{-14} 10^{-13} 10^{-12}
Frequency (kHz)
Narrowband electromagnetic emissions
Electron plasma oscillations at f_p
Upper cutoff at f_p
Auroral hiss
Auroral hiss
UT 03:10 03:15 03:20 03:25 03:30 03:35 03:40 03:45
R_S 1.49 1.54 1.59 1.65 1.71 1.78 1.84 1.91
Lat 13.47 12.47 11.45 10.42 9.41 8.43 7.49 6.59
LT 20.43 20.77 21.09 21.38 21.65 21.90 22.13 22.35
July 1, Day 183, 2004

Figure 28. Top view of the Cassini trajectory during the insertion into the Saturn system. The time range in which auroral hiss emissions were detected is labeled.

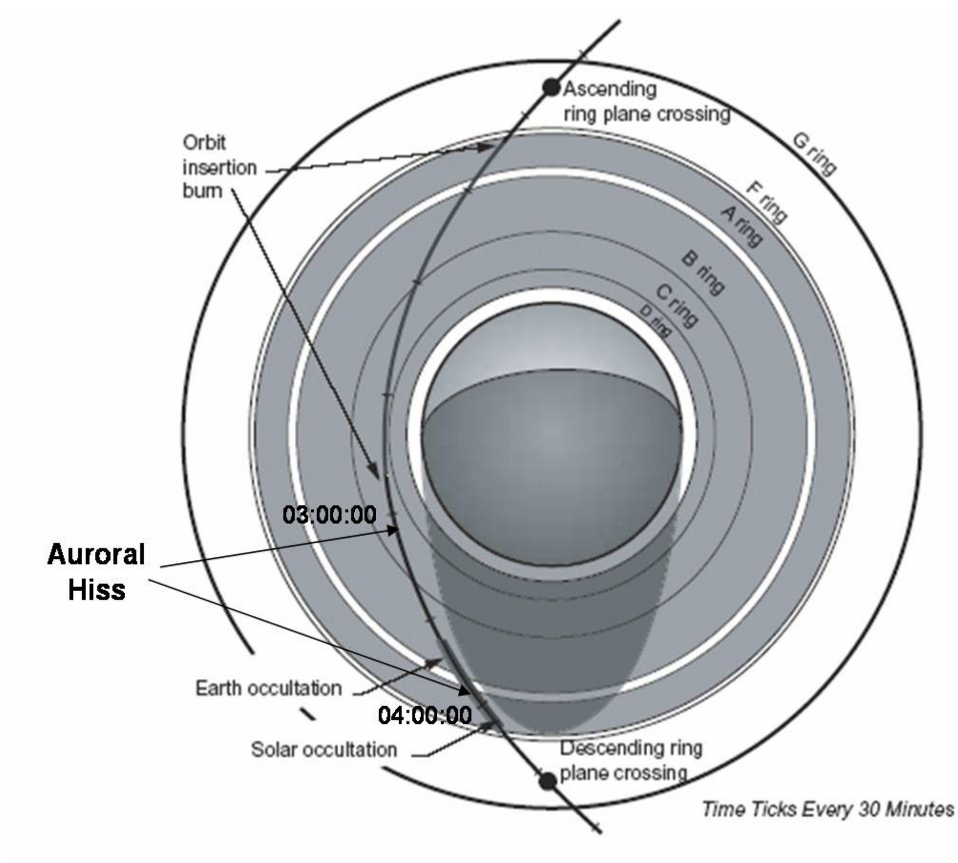
Ascending
ring plane crossing
G ring
F ring
A ring
B ring
C ring
D ring
Orbit
insertion
burn
03:00:00
Auroral
Hiss
Earth occultation
04:00:00
Solar occultation
Descending ring
plane crossing
Time Ticks Every 30 Minutes

Figure 29. Fit (red line) to the measured plasma density by tracing the upper cutoff of the auroral hiss emissions (blue line).

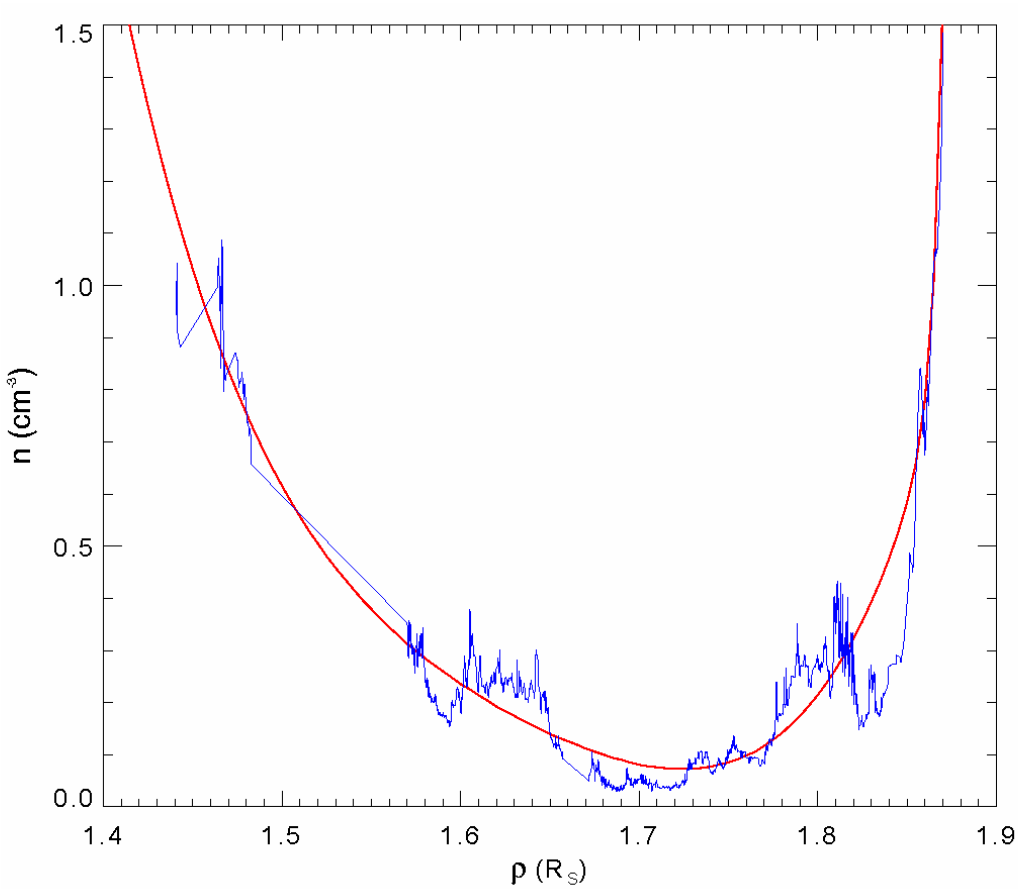

1.5
1.0
0.5
0.0
n (cm⁻³)
1.4
1.5
1.6
1.7
1.8
1.9
ρ (R_S)

Figure 30. Plot of the scale height varying with distance along the equatorial plane.

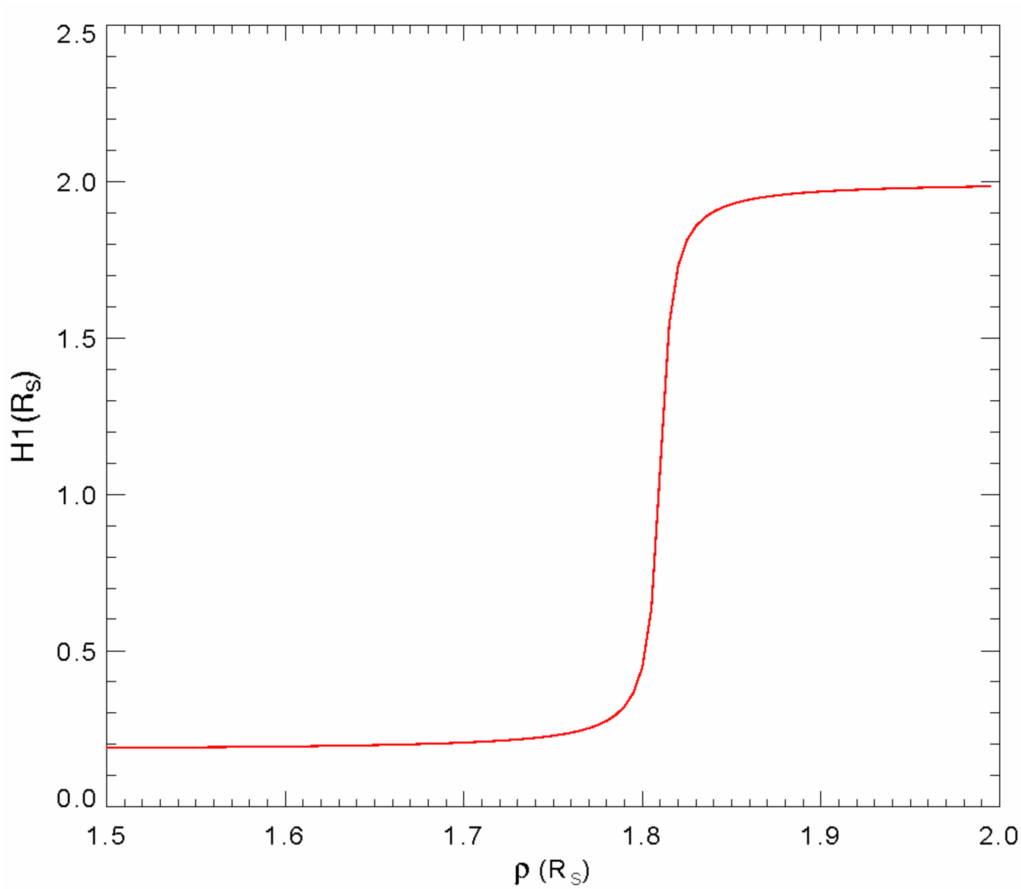

2.5
2.0
1.5
1.0
0.5
0.0
H1(R_S)
1.5
1.6
1.7
1.8
1.9
2.0
ρ (R_S)

Figure 31. Lower cutoff fitting line (gray) based on a source position 1.80 R_S from the Saturn center on the equatorial plane.

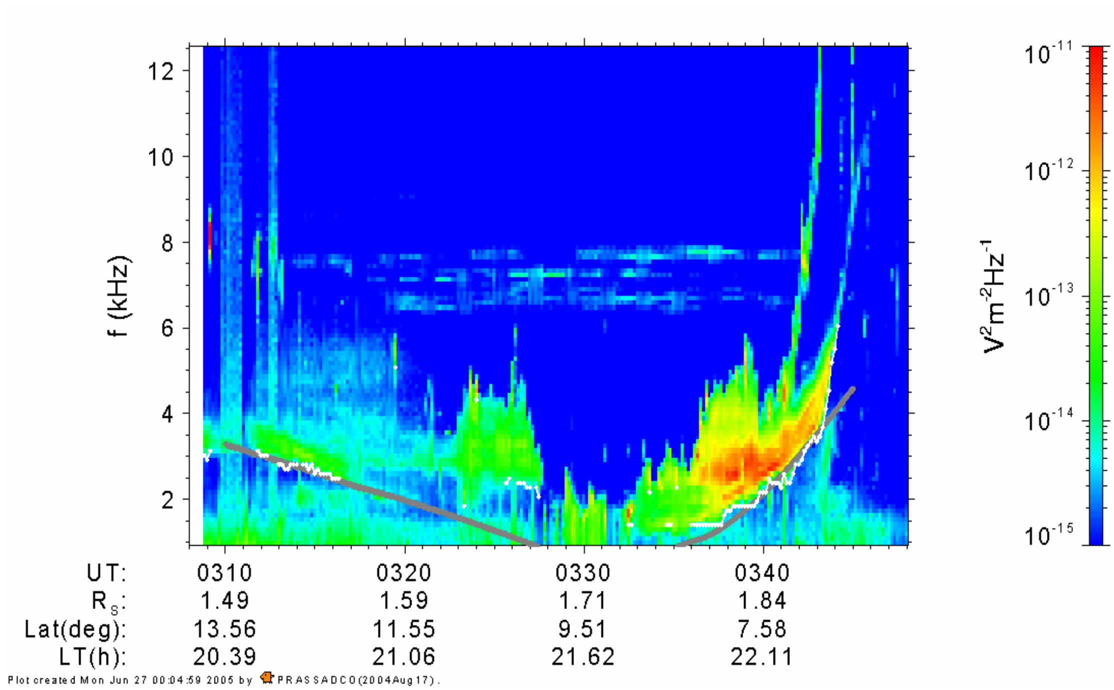

f (kHz)
12
10
8
6
4
2
UT:
0310
0320
0330
0340
R_S:
1.49
1.59
1.71
1.84
Lat(deg):
13.56
11.55
9.51
7.58
LT(h):
20.39
21.06
21.62
22.11
$V^2m^{-2}Hz^{-1}$
10^{-11}
10^{-12}
10^{-13}
10^{-14}
10^{-15}
Plot created Mon Jun 27 00:04:59 2005 by PRASSADCO(2004Aug17).

Figure 32. Demonstration of electron beam acceleration process near Saturn's synchronous orbit point and generation of auroral hiss by electron beams.

A-D04-227-2

Electron Beam Acceleration
Near the Synchronous Orbit Point

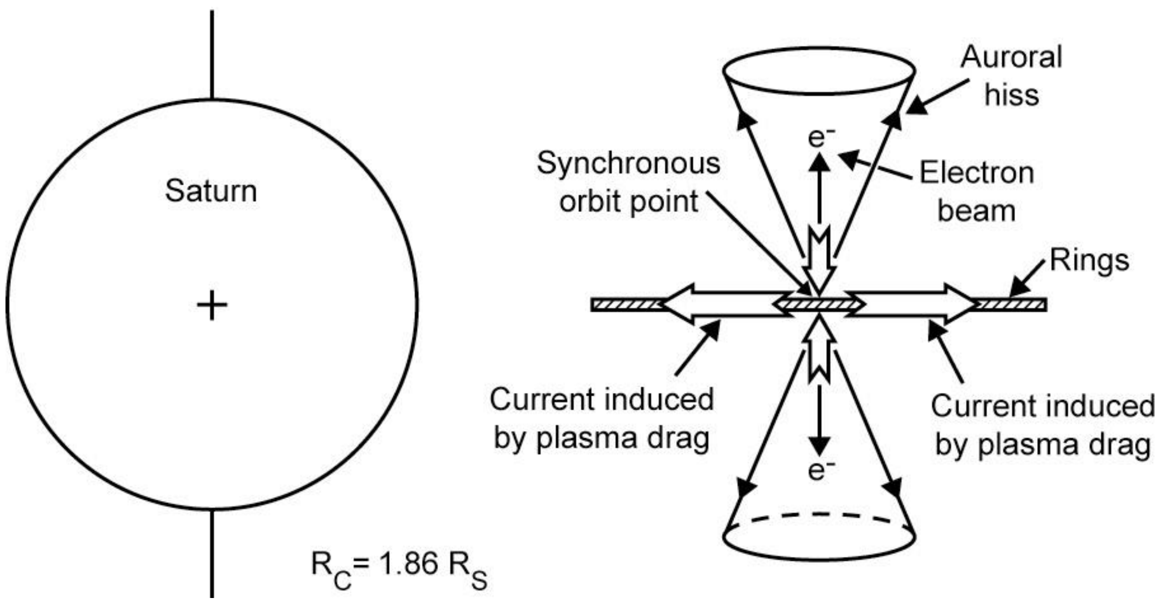

REFERENCES

Bagenal, F., Empirical model of the Io plasma torus: Voyager measurements, *J. Geophys. Res*., **99**, 11,043-11,062, 1994.

Bigg, E.K., Influence of the satellite Io on Jupiter's decametric emission, *Nature*, **203**, 1008, 1964.

Burke, B.F., and K.L. Franklin, Observations of a variable radio source associated with the planet Jupiter, *J. Geophys. Res*., **60**, 213-217, 1955.

Carlson, C.W., J.P. McFadden, R.E. Ergun, M. Temerin, W. Peria, F.S. Mozer, D.M. Klumpar, E.G. Shelley, W.K. Peterson, E. Moebius, R. Elphic, R. Strangeway, C.A. Cattell, and R. Pfaff, FAST observations in the downward auroral current region: energetic upgoing electron beams, parallel potential drops, and ion heating, *Geophys. Res. Lett.*, **25**, 2017-2020, 1998.

Carr, T.D., M.D. Desch, and J.K. Alexander, Phenomenology of magnetospheric radio emissions, in *Physics of the Jovian Magnetosphere*, ed. by A.J. Dessler, Cambridge University Press, London, 1983.

Drell, S.D., H.M. Foley, and M.A. Ruderman, Drag and propulsion of large satellites in the ionosphere: An Alfven propulsion engine in space, *J. Geophys. Res*., **70**, 3131-3146, 1965.

Farrell, W.M., and D.A. Gurnett, An analysis of whistler mode radiation from the Spacelab 2 electron beam, *J. Geophys. Res*., **93**, 153-161, 1988.

Farrell, W.M., D.A. Gurnett, and C.K. Goertz, Coherent Cerenkov radiation from the Spacelab 2 electron beam, *J. Geophys. Res*., **94**, 443-452, 1989.

Farrell, W.M., R.J. MacDowall, R.A. Hess, M.L. Kaiser, M.D. Desch, and R.G. Stone, An interpretation of the broadband VLF waves near the Io torus as observed by Ulysses, *J. Geophys. Res*., **98**, 21,177-21,188, 1993.

Goldreich, P., and Donald Lynden-Bell, Io, a Jovian unipolar inductor, *Astrophys. J*., **156**, 59, 1969.

Gurnett, D.A., High-latitude geophysical studies with satellite Injun 3, *J. Geophys. Res*., **69**, 65-89, 1964.

Gurnett, D.A., A satellite study of VLF hiss, *J. Geophys. Res*., **71**, 5599-5615, 1966.

Gurnett, D.A., Sheath effects and related charged-particle acceleration by Jupiter's satellite Io, *Astrophys. J*., **175**, 525-533, 1972.

Gurnett, D.A., and A. Bhattacharjee, *Introduction to Plasma Physics with Space and Laboratory Applications*, Cambridge University Press, 2005.

Gurnett, D.A., and L.A. Frank, VLF hiss and related plasma observations in the polar magnetosphere, *J. Geophys. Res*., **77**, 172, 1972.

Gurnett, D.A., and W.S. Kurth, Auroral hiss observed near the Io plasma torus, *Nature*, **280**, 767, 1979.

Gurnett, D.A., W.S. Kurth, G.B. Hospodarsky, A.M. Persoon, T.F. Averkamp, B. Cecconi, A. Lecacheux, P. Zarka, P. Canu, N. Cornilleau-Wehrlin, P. Galopeau, A. Roux, C. Harvey, P. Louarn, R. Bostrom, G. Gustafsson, J.-E. Wahlund, M.D. Desch, W.M. Farrell, M.L. Kaiser, K. Goetz, P.J. Kellogg, G. Fischer, H.-P. Ladreiter, H. Rucker, H. Alleyne and A. Pedersen, Radio and plasma wave observations at Saturn from Cassini's approach and first orbit, *Science*, **307**, 1255-1259, 2005.

Gurnett, D.A., W.S. Kurth, J.T. Steinberg, P.M. Banks, R.I. Bush, and W.J. Raitt, Whistler-mode radiation from the Spacelab 2 electron beam, *Geophys. Res. Lett.*, **13**, 225, 1986.

Gurnett, D.A., and F.L. Scarf, Plasma waves in the Jovian magnetosphere, in *Physics of the Jovian Magnetosphere*, edited by A.J. Dessler, pp. 285-316, Cambridge University Press, New York, 1983.

Gurnett, D.A., S.D. Shawhan, and R.R. Shaw, Auroral hiss, Z mode radiation, and auroral kilometric radiation in the polar magnetosphere: DE 1 observations, *J. Geophys. Res*., **88**, 329-340, 1983.

Hill, T.W., A.J. Dessler, and F.C. Michel, Configuration of the jovian magnetosphere, *Geophys. Res. Lett.*, **1**, 3-6, 1974.

Kivelson, M.G. and C.T. Russell, *Introduction to Space Physics*, Cambridge University Press, New York, 1995.

Kivelson, M.G., K.K. Khurana, R.J. Walker, J. Warnecke, C.T. Russell, J.A. Linker, D.J. Southwood, and C. Polanskey, Io's interaction with the plasma torus: Galileo magnetometer report, *Science*, **274**, 396, 1996.

Kletzing, C.A., and R.B. Torbert, Electron time dispersion, *J. Geophys. Res*., **99**, 2159-2172, 1994.

Kliore, A., D.L. Cain, G. Fjeldbo, B.L. Seidel, and S.I. Rasool, Preliminary results on the atmospheres of Io and Jupiter from the Pioneer 10 S-band occultation experiment, *Science*, **183**, 323-324, 1974.

Lin, C.S., J.L. Burch, S.D. Shawhan, and D.A. Gurnett, Correlation of auroral hiss and upward electron beams near the polar cusp, *J. Geophys. Res*., **89**(A2), 925-935, 1984.

Martin, L.H., R.A. Helliwell, and K.R. Marks, Association between aurorae and very-low-frequency hiss observed at Byrd Station, Antarctica, *Nature*, **187**, 751-753, 1960.

Moncuquet, M., A. Lecacheux, N. Meyer-Vernet, B. Cecconi and W.S. Kurth, Quasi thermal noise spectroscopy in the inner magnetosphere of Saturn with Cassini/RPWS: Electron temperatures and density, *Geophys. Res. Lett.*, , in press 2005.

Morgan, D.D., D.A. Gurnett, W.S. Kurth, and F. Bagenal, The source of Jovian auroral hiss observed by Voyager, *J. Geophys. Res*., **99**, 21,213, 1994.

Ness, N.F., M.H. Acuna, R.P. Lepping, L.F. Burlaga, K.W. Behannon, and F.M. Neubauer, Magnetic field studies at Jupiter by Voyager 1: Preliminary results, Science, **203**, 42-46, 1979.

Neubauer, F.M., Nonlinear standing Alfven wave current system at Io: theory, J. *Geophys. Res.*, **85**, 1171-1178, 1980.

Persoon, A.M., D.A. Gurnett, and S.D. Shawhan, Polar cap electron densities from DE 1 plasma wave observations, *J. Geophys. Res*., **88**, 10,123, 1983.

Richardson, J.D., and S. Jurac. A self-consistent model of plasma and neutrals at Saturn: The ion tori, *Geophys. Res. Lett*., **31**, L24803, doi:10.1029/2004GL020959, 2004.

Stix, T.H., *The Theory of Plasma Waves*, McGraw-Hill, New York, 1992.

Storey, L.R.O., An investigation of whistling atmospherics, *Phil. Trans. Roy. Soc. London*, **A, 246**, 113-141, 1953.

Taylor, W.W.L., and S.D. Shawhan, A test of incoherent Cerenkov radiation for VLF hiss and other magnetospheric emissions, *J. Geophys. Res*., **79**, 105, 1974.